Tri-Polarized Holographic MIMO Surfaces for Near-Field Communications: Channel Modeling and Precoding Design

Li Wei, *Graduate Student Member, IEEE*, Chongwen Huang, *Member, IEEE*, George C. Alexandropoulos, *Senior Member, IEEE*, Zhaohui Yang, *Member, IEEE*, Jun Yang, Wei E. I. Sha, *Senior Member, IEEE*, Zhaoyang Zhang, *Senior Member, IEEE*, Mérouane Debbah, *Fellow, IEEE*, and Chau Yuen, *Fellow, IEEE*

***Abstract*— This paper investigates the utilization of triple polarization (TP) for multi-user (MU) wireless communication systems with holographic multiple-input multi-output surfaces (HMIMOSs), targeting capacity boosting and diversity exploitation without enlarging the antenna array sizes of the transceivers. We specifically consider that both the transmitter and receiver are equipped with an HMIMOS consisting of compact sub-wavelength TP patch antennas and operating in the near-field (NF) regime. To characterize TP MU-HMIMOS systems, a TP NF channel model is constructed using the dyadic Green's function, whose characteristics are leveraged to design two precoding schemes for mitigating the cross-polarization and inter-user interference contributions. Specifically, a user-cluster-based precoding scheme that assigns different users to one of three polarizations, at the expense of system's diversity, is presented together with a two-layer precoding technique that removes interference using a Gaussian elimination method. A theoretical correlation analysis for HMIMOS-based systems operating in the NF region is also derived, revealing that both the spacing of transmit patch antennas and user distance impact transmit correlation factors. Our numerical results showcase that the users located far from the transmit HMIMOS experience higher correlation than those closer in the NF region, resulting in a lower channel capacity. In terms of channel capacity, it is demonstrated that the proposed TP HMIMOS-based systems almost achieve 1.25 and 3 times larger gain compared to their dual-polarized version and conventional HMIMOS systems, respectively. It is also shown that the the proposed two-layer precoding scheme combined with two-layer power allocation realizes the highest spectral efficiency, among compared schemes, without sacrificing diversity.**

***Index Terms*— Channel modeling, holographic MIMO surface, near-field communications, full polarization, precoding design, spectral efficiency.**

Manuscript received 31 October 2022; revised 6 February 2023; accepted 31 March 2023. Date of publication 17 April 2023; date of current version 12 December 2023. This work was supported in part by the China National Key Research and Development Program under Grant 2021YFA1000500; in part by the National Natural Science Foundation of China under Grant 62101492; in part by the Zhejiang Provincial Natural Science Foundation of China under Grant LR22F010002; in part by the National Natural Science Fund for Excellent Young Scientists Fund Program (Overseas); in part by the Ng Teng Fong Charitable Foundation in the form of ZJU-SUTD Innovation, Design and Entrepreneurship Alliance (IDEA) Grant; in part by the Zhejiang University Education Foundation; in part by the Qizhen Scholar Foundation; in part by the Fundamental Research Funds for the Central Universities under Grant 2021FZZX001-21; in part by the Smart Networks and Services Joint Undertaking TERahertz ReconfigurAble METAsurfaces (SNS JU TERRAMETA) Project under EU's Horizon Europe Research and Innovation Programme under Grant 101097101; and in part by the Ministry of Education (MOE), Singapore, through its MOE Tier 2 under Award MOE-T2EP50220-0019. The associate editor coordinating the review of this article and approving it for publication was C.-K. Wen. *(Corresponding author: Chongwen Huang.)*

Li Wei is with the Engineering Product Development (EPD) Pillar, Singapore University of Technology and Design, Singapore 487372 (e-mail: wei_li@mymail.sutd.edu.sg).

Chongwen Huang, Zhaohui Yang, and Zhaoyang Zhang are with the College of Information Science and Electronic Engineering, Zhejiang University, Hangzhou 310027, China, also with the International Joint Innovation Center, Zhejiang University, Haining 314400, China, and also with the Zhejiang Provincial Key Laboratory of Information Processing, Communication and Networking (IPCAN), Hangzhou 310027, China (e-mail: chongwenhuang@zju.edu.cn; zhaohui_yang@zju.edu.cn; ning_ming@zju.edu.cn).

George C. Alexandropoulos is with the Department of Informatics and Telecommunications, National and Kapodistrian University of Athens, 15784 Athens, Greece (e-mail: alexandg@di.uoa.gr).

Jun Yang is with the State Key Laboratory of Mobile Network and Mobile Multimedia Technology, Shenzhen 518055, China, and also with the Wireless Product Research and Development Institute, ZTE Corporation, Shenzhen 518057, China (e-mail: yang.jun10@zte.com.cn).

Wei E. I. Sha is with the College of Information Science and Electronic Engineering, Zhejiang University, Hangzhou 310027, China (e-mail: weisha@zju.edu.cn).

Mérouane Debbah is with the Technology Innovation Institute, Masdar City, Abu Dhabi, United Arab Emirates, and also with Centrale Supélec, University Paris-Saclay, 91192 Gif-sur-Yvette, France (e-mail: merouane.debbah@tii.ae).

Chau Yuen is with the School of Electrical and Electronics Engineering, Nanyang Technological University, Singapore 639798 (e-mail: chau.yuen@ntu.edu.sg).

Color versions of one or more figures in this article are available at https://doi.org/10.1109/TWC.2023.3266298.

Digital Object Identifier 10.1109/TWC.2023.3266298

I. Introduction

THE explosive development of mobile devices and multimedia applications appeals for powerful wireless communication techniques to provide larger bandwidths and higher throughput. Some communication technologies are employed to increase the capacity of wireless communications, e.g., TeraHertz [1] and millimeter-Wave communications [2], as well as extreme multiple-input multiple-output (MIMO) [3], [4], [5], [6]. However, the massive data traffic and high reliability of wireless communications still pose serious challenges to algorithmic and hardware designs.

Holographic MIMO surface (HMIMOS), an evolution of reconfigurable intelligent surface (RIS), provides feasible and engaging research directions toward realizing highly flexible

1536-1276 © 2023 IEEE. Personal use is permitted, but republication/redistribution requires IEEE permission.
See https://www.ieee.org/publications/rights/index.html for more information.

Authorized licensed use limited to: Zhejiang University. Downloaded on December 14,2023 at 13:10:36 UTC from IEEE Xplore. Restrictions apply.

antennas by intelligently leveraging electromagnetic (EM) waves [7], [8], [9], [10], [11], [12], [13]. Specifically, an HMIMOS consists of almost infinite antennas in compact size achieves spatially continuous aperture [14], [15], and it is verified to have many merits. For example, the work in [7] proved theoretically the flexibility of HMIMOS configuration and its advantages in improving spectral efficiency. The authors in [16] showed that large RISs can achieve super-directivity. Benefiting from these merits, HMIMOS can be applied in many scenarios, such as wireless power transfer and indoor positioning [7], [17]. However, the full exploitation of this technology is still infeasible due to various non-trivial technical issues.

The main challenge of the HMIMOS technology is the constrained performance gain that depends on array size. Since an HMIMOS incorporates large amount of patch antennas with sub-wavelength inter-element spacing in a small area, there exists strong correlation between the patch antennas, which degrades the performance [18], [19], [20], [21]. In fact, stronger correlation is induced when increasing the number of patch antennas added to a fixed surface area (i.e., when the inter-element spacing is reduced). In fact, it has been proved that the degrees of freedom (DoF) brought by increasing the number of patch antennas are limited by the size of HMIMOS [22], [23]. However, it is still unknown how to effectively improve the spectral efficiency of an HMIMOS in a given area when its performance limit is reached.

The integration of the dual-polarization (DP) or tripolarization (TP) feature is expected to further improve the performance without enlarging antenna array size, offering polarization diversity which can boost spectral efficiency [24], [25]. Inspired by the favorable performance gain brought by polarization techniques, a few recent works discussed the deployment of polarized RIS systems [26], [27], [28], [29], [30]. A DP RIS-based transmission system to achieve low-cost ultra-massive MIMO transmission was designed in [26]. In [30], an RIS-based wireless communication structure to control the reflected beam and polarization state for maximizing the received signal power was proposed. Nevertheless, there are still open challenges in polarized wireless communications.

The primary difficulty of wireless systems using polarization is channel modeling. There are mainly two types of EM assumptions in channel modeling, i.e., the near-field (NF) and far-field assumptions. The former regime is characterized by TP, while the latter by DP, since one of the polarizations vanishes in the transition from the NF to the far-field region. Differently from conventional channel models that exploit only a single polarization, the polarized channel involves additional components, i.e., the co-polarized and cross-polarized channels. Besides, for polarized channel, there exists an interplay between spatial and polarization correlation [31]. Thus, the conventional independent and identically distributed assumption cannot be directly adopted to model co-/cross-polarized channels [27]. However, in most of the existing literature, the powers of the co-polarized channels are assumed to be equal [28], [29], and the power allocation is ignored [32], which can hardly happen in practice. Therefore, a realistic polarized channel model is required.

The interference elimination in polarized systems is a difficult task. In particular, both spatial and cross-polarization interferences have destructive impacts on the system performance [15], [33]. The former comes from the closely placed antennas, while the latter stems from the interplay between the co-polarization and cross-polarization components. There are only a few works dealing with polarization interference elimination in wireless communications. For example, [24] eliminated the cross-polarization component in DP multi-user (MU) communications by performing successive interference cancellation in each user cluster. In addition, the higher gain brought in TP systems gets along with the more complex cross-polarization interference. Specifically, the sum of two cross-polarization components jointly influences the performance of TP systems, which is different from the single cross-polarization component in DP systems.

In order to exploit the potential of polarized MU HMIMOS-based wireless communications, this paper presents a TP MU-HMIMOS channel model for the NF regime, which is employed to design a user-cluster-based precoding scheme and a two-layer precoding technique aiming at mitigating interference and handling power imbalance. The proposed channel model is proved to be efficient enough through both a novel theoretical analysis and extensive numerical results. It is, particularly, showcased for the investigated NF regime that TP HMIMOS-based systems are more efficient than DP and conventional HMIMOS-based systems, and that users located closer to the transmit HMIMOS exhibit lower correlation than those being far from it. The main contributions of this paper are summarized as follows:

- Building on the dyadic Green's function, we present a NF channel model of MU HMIMOS-based communication systems that captures TP characteristics. Specifically, both transmit and receive HMIMOSs are divided into many small pieces and we adopt two Fraunhofer assumptions to approximate their NF channel. The assumptions are then proved to be applicable in the considered scenario.
- To combat the cross-polarization and inter-user interference contributions in the considered TP HMIMOS-based systems, we propose two precoding schemes for MU operation. The first scheme is a user-cluster-based precoding employing one-third of the available diversity to alleviate interference, while the second one relies on a two-layer precoding based on the Gaussian elimination and block diagonalization (BD) to remove interference. In addition, a two-layer power allocation (PA) method is presented to manage the power imbalance, which is shown to achieve higher spectral efficiency.
- A novel theoretical correlation analysis is presented to substantiate the practicality of the proposed channel model. It is particularly shown that the spacing of patch antennas and the distance between transmit and receive HMIMOS determine correlation. Our simulation results reveal that, not only the number of transmit antennas has

Authorized licensed use limited to: Zhejiang University. Downloaded on December 14,2023 at 13:10:36 UTC from IEEE Xplore. Restrictions apply.

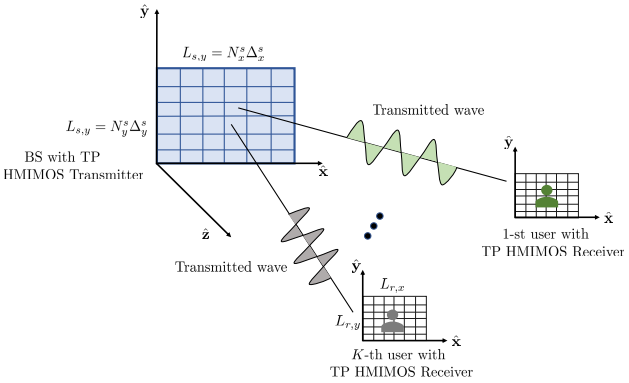

Fig. 1. The considered TP MU-HMIMOS downlink communication system consisting of a BS with N_s patch antennas serving K users, each equipped with $\bar{N}_r$ patch antennas.

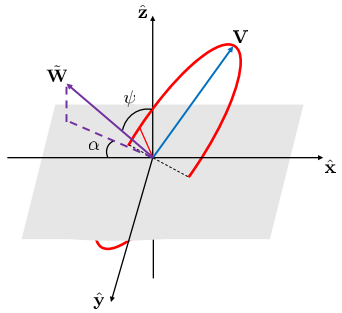

Fig. 2. Elliptic polarization state generated by TP HMIMOS.

the significant impact on the degree of freedom (DoF), but also the shape of the HMIMOS affects it. The performance of proposed precoding schemes is extensively compared with alternative PA strategies.

The remainder of this paper is organized as follows. In Section II, the TP MU-HMIMOS system model and polarization generation are introduced. The NF channel model for TP MU-HMIMOS using Green's function is presented in Section III. Section IV presents two precoding schemes to eliminate interference. A two-layer PA method is discussed in Section V. Section VI presents the theoretical analysis and numerical results of the TP MU-HMIMOS performance. Finally, conclusions are drawn in Section VII.

Notation: Fonts a, $\mathbf{a}$, and $\mathbf{A}$ represent scalars, vectors, and matrices, respectively. $\mathbf{A}^T$, $\mathbf{A}^\dagger$, $\mathbf{A}^{-1}$, and $\|\mathbf{A}\|_f$ denote transpose, Hermitian (conjugate transpose), inverse (pseudo-inverse), and Frobenius norm of $\mathbf{A}$, respectively. $\mathbf{A}_{i,j}$ or $[\mathbf{A}]_{i,j}$ represents $\mathbf{A}$'s (i,j)th element. $\mathrm{tr}(\cdot)$ gives the trace of a matrix, $\mathbf{I}_n$ (with $n \geq 2$) is the $n \times n$ identity matrix. $\delta_{k,i}$ equals to 1 when $k = i$ or 0 when $k \neq i$. Finally, notation $\mathrm{diag}(\mathbf{a})$ represents a diagonal matrix with the entries of $\mathbf{a}$ on its main diagonal, and $\mathrm{blkdiag}[\mathbf{A}_1, \ldots, \mathbf{A}_N]$ is the block diagonal matrix created by matrices $\mathbf{A}_1, \ldots, \mathbf{A}_N$ along the diagonal.

II. TP MU-HMIMOS

A. System Model

In the considered TP MU-HMIMOS communication system, the BS is equipped with an HMIMOS of size $A_s = L_{s,x} \times L_{s,y}$ where $L_{s,x}$ and $L_{s,y}$ denote surfaces' horizontal and vertical lengths, respectively, and the K users have also a TP HMIMOS of size $A_r = L_{r,x} \times L_{r,y}$ with $L_{r,x}$ and $L_{r,y}$ being their common horizontal and vertical lengths, respectively. The HMIMOSs at the BS and each of the users are composed of N_s and $\bar{N}_r$ patch antennas, respectively. Thus, the sum of the receive patch antennas in the downlink is $N_r = K\bar{N}_r$. Each patch antenna is made from metamaterials that are capable of independently adjusting their reflection coefficients in three polarizations [3], [26], [34], as shown in Fig. 1. We represent the phase configuration matrix (i.e., the analog beamforming) of the HMIMOS at the BS by the block-diagonal matrix $\mathbf{\Phi}^s \in \mathbb{C}^{3N_s \times 3N_s}$, whose non-zero blocks $\mathbf{\Phi}_n^s \in \mathbb{C}^{3\times 3}$, with $n = 1, 2, \ldots, N_s$, refer to the three-polarization configuration of each nth patch antenna. Each of these configurations is represented by the following diagonal matrix:

$$\mathbf{\Phi}_n^s = \mathrm{diag}[E_{n,x}^s e^{j\theta_{n,x}^s}, E_{n,y}^s e^{j\theta_{n,y}^s}, E_{n,z}^s e^{j\theta_{n,z}^s}], \quad (1)$$

where $\theta_{n,x}^s, \theta_{n,y}^s$, and $\theta_{n,z}^s \in [0, 2\pi]$ are three independent phase shifts in the excited triple polarization states, with $E_{n,x}^s, E_{n,y}^s$, and $E_{n,z}^s \in [0,1]$ denoting the corresponding amplitude reflection coefficients at the nth patch antenna.

Assuming that the EM wave propagates towards the $\hat{\mathbf{z}}$ direction, thus, it can be decomposed into the components $(E_x(t), E_y(t), E_z(t))$ in three orthogonal directions, i.e., in $\hat{\mathbf{x}}$, $\hat{\mathbf{y}}$, and $\hat{\mathbf{z}}$ directions, the instantaneous electrical field is

$$\mathbf{E}(t) = E_x(t)\hat{\mathbf{x}} + E_y(t)\ \hat{\mathbf{y}} + E_z(t)\hat{\mathbf{z}}, \quad (2)$$

where $E_j(t) \triangleq E_j \exp(i(\omega t + \theta_{n,j}))$ with $j \in \{x, y, z\}$, and $(\theta_{n,x}, \theta_{n,y}, \theta_{n,z})$ are the phases of the three polarized components that are controlled by each nth patch antenna in the HMIMOS. In the sequel, the term t referring to the dependence in time is omitted for simplicity, i.e., $E(t)$ becomes E in the following.

B. Generated Polarization Ellipse

The conjoint characteristics of three polarized wave components (E_x, E_y, E_z) determine a general elliptical polarization, as shown in Fig. 2.

The elliptical polarization plane and and spectral density are all controlled by HMIMOS, and these information can be exploited in information exchange, such as encoding and precoding [35]. Specifically, the polarization plane's normal vector $\tilde{\mathbf{W}} = (\tilde{\mathbf{W}}_x, \tilde{\mathbf{W}}_y, \tilde{\mathbf{W}}_z)$ is given by [36]

$$\begin{aligned} \tilde{\mathbf{W}}_{n,x} &= -2E_{n,y}E_{n,z}\sin(\theta_{n,y} - \theta_{n,z}), \\ \tilde{\mathbf{W}}_{n,y} &= -2E_{n,z}E_{n,x}\sin(\theta_{n,z} - \theta_{n,x}), \\ \tilde{\mathbf{W}}_{n,z} &= -2E_{n,x}E_{n,y}\sin(\theta_{n,x} - \theta_{n,y}), \end{aligned} \quad (3)$$

and the spectral density tensor is given by

$$\mathbf{S}_d = \begin{pmatrix} E_x^2 & E_xE_ye^{i\vartheta_{xy}} & E_xE_ze^{i\vartheta_{xz}} \\ E_yE_xe^{-i\vartheta_{xy}} & E_y^2 & E_yE_ze^{i\vartheta_{yz}} \\ E_zE_xe^{-i\vartheta_{xz}} & E_zE_ye^{-i\vartheta_{yz}} & E_z^2 \end{pmatrix}, \quad (4)$$

with $\vartheta_{ij} = \theta_i - \theta_j$ is the phase difference between two polarized waves. In this work, we assume that the initial phase

Authorized licensed use limited to: Zhejiang University. Downloaded on December 14,2023 at 13:10:36 UTC from IEEE Xplore. Restrictions apply.

setting in the three polarization states is the same, resulting in linearly polarized states.

The pseudovector of the spectral density tensor is given by $\mathbf{V} = (\mathbf{\Lambda}_7, -\mathbf{\Lambda}_5, \mathbf{\Lambda}_2)$ [37], i.e.,

$$\mathbf{\Lambda}_7 = -2\,\mathrm{Im}\left\{\mathbf{E}_y\mathbf{E}_z^*\right\}, \quad \mathbf{\Lambda}_5 = -2\,\mathrm{Im}\left\{\mathbf{E}_x\mathbf{E}_z^*\right\}, \times \mathbf{\Lambda}_2 = -2\,\mathrm{Im}\left\{\mathbf{E}_x\mathbf{E}_y^*\right\}. \quad (5)$$

The complex vector $\mathbf{E} = (\mathbf{E}_x, \mathbf{E}_y, \mathbf{E}_z)$ and its conjugate vector $\mathbf{E}^*$ form a polarization plane in space, which is the same plane as the polarzation ellipse since $\mathbf{V}$ is perpendicular to $\mathbf{E}$ and $|\mathbf{V}|$ is equal to $2/\pi$ times the area of the polarization ellipse [37]. As shown in Fig. 2, ψ is the angle between the normal vector of polarization plane and the $\hat{\mathbf{z}}$ axis, and the angle α is the angle between the projection of normal vector on xy-plane and $\hat{\mathbf{x}}$ axis. It can be observed that both amplitude and phase shift of HMIMOS determine the polarization parameters.

III. Proposed Near-Field Channel Model

The radiated electric field $\mathbf{E}(\mathbf{r})$ at the location $\mathbf{r} \in \mathbb{R}^3$ in the half free-space, resulting from the current $\mathbf{J}(\mathbf{r}')$, which is generated at the location $\mathbf{r}' \in \mathbb{R}^3$, is given by the dyadic Green's function theorem as follows [22], [38]

$$\mathbf{E}(\mathbf{r}) \triangleq i\omega\mu \int_S ds' \bar{\mathbf{G}}\left(\mathbf{r}, \mathbf{r}'\right) \cdot \mathbf{J}\left(\mathbf{r}'\right), \quad (6)$$

where S denotes the surface of the HMIMOS transmitter, ω is permittivity, and μ is permeability. The dyadic Green's function is defined as [39]:

$$\begin{aligned}\bar{\mathbf{G}}\left(\mathbf{r}, \mathbf{r}'\right) &\triangleq \left[\bar{\mathbf{I}} + \frac{\nabla\nabla}{k_0^2}\right] g\left(\mathbf{r}, \mathbf{r}'\right) \\ &= \left(1 + \frac{i}{k_0 r} - \frac{1}{k_0^2 r^2}\right)\bar{\mathbf{I}} g(\mathbf{r}, \mathbf{r}') \\ &\quad + \left(\frac{3}{k_0^2 r^2} - \frac{3i}{k_0 r} - 1\right)\vec{\mathbf{r}}\vec{\mathbf{r}} g(\mathbf{r}, \mathbf{r}'), \end{aligned} \quad (7)$$

where $\bar{\mathbf{I}}$ is identity matrix, $\nabla\nabla g(\cdot)$ denotes the second-order derivative of function $g(\cdot)$ with respect to its argument, $k_0 \triangleq \frac{2\pi}{\lambda}$ is the wavenumber with λ being the wavelength, and the unit vector $\vec{\mathbf{r}}$ denotes the direction between the source point and radiated field. The scalar Green's function is [39] and [40]:

$$g\left(\mathbf{r}, \mathbf{r}'\right) \triangleq \frac{e^{ik_0|\mathbf{r}-\mathbf{r}'|}}{4\pi|\mathbf{r}-\mathbf{r}'|}. \quad (8)$$

Inspired by the work in [41], which calculates the sound field radiated from a plane source using the scalar Green's function, we derive the dyadic Green's function that takes polarization into consideration. Specifically, the N_s-patch HMIMOS is divided into N_s rectangles, each with size $\Delta^s = \Delta_x^s\Delta_y^s$. Each patch is regarded as a point (x_n', y_n') in a first coordinate system, and is further investigated in a second coordinate system defined within (x_0', y_0') (this is equivalent to the size of each patch antenna). Under this consideration, the electric field can be rewritten as follows:

$$\begin{aligned}\mathbf{E}(\mathbf{r}) &= \sum_{n=1}^{N_s}\int_{\Delta^s} d\mathbf{r}_n' \bar{\mathbf{G}}\left(\mathbf{r}, \mathbf{r}_n'\right) \cdot \mathbf{J}\left(\mathbf{r}_n'\right) \\ &= \sum_{n=1}^{N_s}\int_{-\Delta_x^s/2}^{\Delta_x^s/2}\int_{-\Delta_y^s/2}^{\Delta_y^s/2} dx_0' dy_0' \\ &\quad \times \left[\bar{\mathbf{I}} + \frac{\nabla\nabla}{k_0^2}\right]\frac{e^{ik_0 r_n}}{4\pi r_n}\mathbf{J}\left(\mathbf{r}_n'\right), \end{aligned} \quad (9)$$

with the distance r_n given by:

$$\begin{aligned} r_n = |\mathbf{r} - \mathbf{r}_n'| &= \sqrt{(x - x_n' - x_0')^2 + (y - y_n' - y_0')^2 + z^2} \\ &= \sqrt{(\hat{x}_n - x_0')^2 + (\hat{y}_n - y_0')^2 + z^2}, \end{aligned} \quad (10)$$

where $\hat{x}_n \triangleq x - x_n'$ and $\hat{y} \triangleq y - y_n'$. We henceforth assume, for simplicity, that the current distribution $\mathbf{J}(\mathbf{r}_n') = J_x(\mathbf{r}_n')\hat{\mathbf{x}} + J_y(\mathbf{r}_n')\hat{\mathbf{y}}$ is constant, and $J_x(\mathbf{r}_n') = J_y(\mathbf{r}_n') = 1$.

If Δ_x^s and Δ_y^s are infinitely small, the distance to the field point (i.e., the receiver) is much greater than the dimensions of the source, hence, the Fraunhofer approximation can be adopted, i.e., $\sqrt{{x_0'}^2 + {y_0'}^2}/\tilde{R}_n \approx (0, 0)$, where $\tilde{R}_n$ is:

$$\tilde{R}_n = \sqrt{(x - x_n')^2 + (y - y_n')^2 + z^2} = \sqrt{\hat{x}_n^2 + \hat{y}_n^2 + z^2}. \quad (11)$$

In this case, the distance $\tilde{r}_n$ from the nth transmit patch antenna in the exponential term is approximated by:

$$\begin{aligned}\tilde{r}_n &= \sqrt{(\hat{x}_n - x_0)^2 + (\hat{y}_n - y_0)^2 + z^2} \\ &\overset{(a)}{\approx} \tilde{R}_n - \frac{\hat{x}_n x_0'}{\tilde{R}_n} + \frac{{x_0'}^2}{2\tilde{R}_n} - \frac{\hat{y}_n y_0'}{\tilde{R}_n} + \frac{{y_0'}^2}{2\tilde{R}_n} + \tilde{R}_n\mathcal{O}\left(u(\mathbf{r}, \mathbf{r}_n')\right) \\ &\overset{(b)}{\approx} \tilde{R}_n - \frac{\hat{x}_n x_0'}{\tilde{R}_n} - \frac{\hat{y}_n y_0'}{\tilde{R}_n}, \end{aligned} \quad (12)$$

where (a) is Taylor series expansion, and $u(\mathbf{r}, \mathbf{r}_n') = \frac{2\hat{x}_n x_0'}{\tilde{R}_n^2} - \frac{{x_0'}^2}{\tilde{R}_n^2} + \frac{2\hat{y}_n y_0'}{\tilde{R}_n^2} - \frac{{x_0'}^2}{\tilde{R}_n^2}$, with $\mathcal{O}\left(u(\mathbf{r}, \mathbf{r}_n')\right)$ being the negligible higher order terms. In addition, (b) results from the fact that the term $\left|\frac{\sqrt{{x_0'}^2 + {y_0'}^2}}{2\tilde{R}_n}\right|$ is small.

By making the reasonable assumption that $1/r_n \approx 1/\tilde{R}_n$, the radiated electric field from the nth transmitting patch antenna can be obtained as follows:

$$\begin{aligned}\mathcal{E}(\tilde{R}_n) &= \sum_{n=1}^{N_s}\int_{-\Delta_x^s/2}^{\Delta_x^s/2}\int_{-\Delta_y/2}^{\Delta_y^s/2} dx_0' dy_0' \frac{e^{ik_0|\mathbf{r}-\mathbf{r}_n'|}}{4\pi\tilde{R}_n} \\ &= \sum_{n=1}^{N_s}\int_{-\Delta_x^s/2}^{\Delta_x^s/2}\int_{-\Delta_y^s/2}^{\Delta_y^s/2} dx_0' dy_0' \tilde{\mathbf{G}}(\hat{x}_n, \hat{y}_n; x_0', y_0'), \end{aligned} \quad (13)$$

where we have used the function definition:

$$\begin{aligned}\tilde{\mathbf{G}}(\hat{x}_n, \hat{y}_n; x_0', y_0') &= \frac{\exp\{ik_0\left[\tilde{R}_n - \frac{\hat{x}_n x_0'}{\tilde{R}_n} - \frac{\hat{y}_n y_0'}{\tilde{R}_n}\right]\}}{4\pi\tilde{R}_n} \\ &= \frac{e^{ik_0\tilde{R}_n}}{4\pi\tilde{R}_n}\exp\left(ik_0\left[-\frac{\hat{x}_n x_0'}{\tilde{R}_n}\right]\right) \\ &\quad \times \exp\left(ik_0\left[-\frac{\hat{y}_n y_0'}{\tilde{R}_n}\right]\right). \end{aligned} \quad (14)$$

Authorized licensed use limited to: Zhejiang University. Downloaded on December 14,2023 at 13:10:36 UTC from IEEE Xplore. Restrictions apply.

Using the notation $\Delta^s = \Delta_x^s \Delta_y^s$ and $\mathrm{sinc}(x) = \frac{\sin x}{x}$, the last integral in (13) can be solved as follows:

$$\mathcal{E}(\tilde{R}_n) = \sum_{n=1}^{N_s} \int_{-\frac{\Delta_x^s}{2}}^{\frac{\Delta_x^s}{2}} \int_{-\frac{\Delta_y^s}{2}}^{\frac{\Delta_y^s}{2}} dx_0' dy_0' \tilde{\mathbf{G}}(\hat{x}_n, \hat{y}_n; x_0', y_0') = \Delta^s \sum_{n=1}^{N_s} \frac{e^{ik_0 \tilde{R}_n}}{4\pi \tilde{R}_n} \mathrm{sinc}\, \frac{k_0 \hat{x}_n \Delta_x^s}{2\tilde{R}_n} \mathrm{sinc}\, \frac{k_0 \hat{y}_n \Delta_y^s}{2\tilde{R}_n}. \quad (15)$$

By making use of the following two terms given in (7):

$$c_1(\tilde{R}_n) = \left(1 + \frac{i}{k_0 \tilde{R}_n} - \frac{1}{k_0^2 \tilde{R}_n^2}\right), \; c_2(\tilde{R}_n) = \left(\frac{3}{k_0^2 \tilde{R}_n^2} - \frac{3i}{k_0 \tilde{R}_n} - 1\right), \quad (16)$$

the wireless channel with polarization between the nth transmit patch antenna and a receiving point can be written as

$$\mathbf{H}_n = \mathcal{E}(\tilde{R}_n)\mathbf{C}_n = \mathcal{E}(\tilde{R}_n)\left(c_1(\tilde{R}_n)\mathbf{I} + c_2(\tilde{R}_n)\vec{\mathbf{r}}_n \vec{\mathbf{r}}_n\right), \quad (17)$$

where the unit vector $\vec{\mathbf{r}}_n \triangleq \frac{\mathbf{r} - \mathbf{r}_n'}{r_n}$ denotes the direction of each receive-transmit patch-antenna pair.

A. Channel Matrix and Feasibility

It is, in general, expected that the receive HMIMOS will be much smaller than the transmit one, hence, it is reasonable to assume that the power received by each patch antenna will be proportional to the receive area $\Delta^r \triangleq \Delta_x^r \Delta_y^r$. Therefore, the channel between each mth, with $m = 1, 2, \ldots, \bar{N}$, receive and each nth transmit patch antennas can be expressed as:

$$\mathbf{H}_{mn} = \Delta^s \Delta^r \frac{e^{(ik_0 \tilde{R}_{mn})}}{4\pi \tilde{R}_{mn}} \mathrm{sinc}\, \frac{k_0 (x_m - x_n') \Delta_x^s}{2\tilde{R}_{mn}} \cdot \mathrm{sinc}\, \frac{k_0 (y_m - y_n') \Delta_y^s}{2\tilde{R}_{mn}} \mathbf{C}_{mn} = \begin{bmatrix} cH_{mn}^{xx}, & H_{mn}^{xy}, & H_{mn}^{xz} \\ H_{mn}^{yx}, & H_{mn}^{yy}, & H_{mn}^{yz} \\ H_{mn}^{zx}, & H_{mn}^{zy}, & H_{mn}^{zz} \end{bmatrix}, \quad (18)$$

where $\mathbf{C}_{mn} \triangleq c_1(\tilde{R}_{mn})\mathbf{I} + c_2(\tilde{R}_{mn})\vec{\mathbf{r}}_{mn}\vec{\mathbf{r}}_{mn} \in \mathbb{C}^{3\times 3}$. The overall channel matrix can be thus represented as follows:

$$\mathbf{H} = \begin{bmatrix} \mathbf{H}_{xx} & \mathbf{H}_{xy} & \mathbf{H}_{xz} \\ \mathbf{H}_{yx} & \mathbf{H}_{yy} & \mathbf{H}_{yz} \\ \mathbf{H}_{zx} & \mathbf{H}_{zy} & \mathbf{H}_{zz} \end{bmatrix} \in \mathbb{C}^{3N_r \times 3N_s}, \quad (19)$$

where $\mathbf{H}_{pq} \in \mathbb{C}^{N_r \times N_s}$, with $p, q \in \{x, y, z\}$, denotes the polarized channel that collects all channel components transmitted in the pth polarization and received in the qth polarization. We will next prove the validity of our two core assumptions following our proposed channel model.

Recall that, in order to derive the above expressions, we have used the following two approximations:

- $\exp\left(ik\left[-\frac{\hat{x}_n \Delta_x}{2\tilde{R}_n} - \frac{\hat{y}_n \Delta_y}{2\tilde{R}_n}\right]\right) \approx 1$ (or equivalently $\left|\frac{\mathbf{r}_0'}{2\tilde{R}_n}\right| \approx 0$) was adopted in (12), implying that the transmitter patch antenna is small enough compared to twice the distance between the transmitter and receiver;
- $r_n \approx \tilde{R}_n$ was used in the derivation of (13).

Following these assumptions, the length limit of each patch antenna can be deduced. Specifically, since $\exp\left(\frac{ik_0(x_0'^2 + y_0'^2)}{2\tilde{R}_n}\right) \approx 1$, $-\Delta_x^s \le x_0' \le \Delta_x^s$, and $-\Delta_y^s \le y_0' \le \Delta_y^s$, it holds $\cos\left(\frac{k_0(\Delta_x^{s\,2} + \Delta_y^{s\,2})}{8\tilde{R}_n}\right) \approx 1$. Thus, $\frac{k_0(\Delta_x^{s\,2} + \Delta_y^{s\,2})}{8\tilde{R}_n} \ll \pi$, or equivalently, $\frac{k_0 \Delta_x^{s\,2}}{8\tilde{R}_n} \ll \pi$ and $\frac{k_0 \Delta_y^{s\,2}}{8\tilde{R}_n} \ll \pi$. Therefore, the limitation on the patch antenna sizes at the receiver and transmitter is

$$\Delta_x^r \le \Delta_x^s \ll 2\sqrt{\lambda \tilde{R}_n}, \quad \Delta_y^r \le \Delta_y^s \ll 2\sqrt{\lambda \tilde{R}_n}. \quad (20)$$

Since the near-field region is determined by condition $r_{\mathrm{NF}} \le \frac{2(D_1 + D_2)^2}{\lambda}$ [42], [43], the aperture at the transmitter is $D_1 = \sqrt{L_{s,x}^2 + L_{s,y}^2}$ and the aperture at the receiver is $D_2 = \sqrt{L_{r,x}^2 + L_{r,y}^2}$. If we consider that $N_{s,x} = N_{s,y} = \sqrt{N_s}$ ($N_{s,x}$ and $N_{s,y}$ are the numbers of horizontal and vertical patch antennas at the BS) and $\bar{N}_{r,x} = \bar{N}_{r,y} = \sqrt{\bar{N}_r}$ ($\bar{N}_{r,x}$ and $\bar{N}_{r,y}$ denote the numbers of the horizontal and vertical patch antennas at each user), the near-field region is deduced:

$$r_{\mathrm{NF}} \le \frac{4N_s(\Delta_x^s)^2 + 4\bar{N}_r(\Delta_x^r)^2 + 8\sqrt{N_s \bar{N}_r}\Delta_x^s \Delta_x^r}{\lambda}. \quad (21)$$

By letting $\tilde{R}_n = r_{\mathrm{NF}}$, the length limit of each patch antenna is

$$(\Delta_x^s)^2 + (\Delta_y^s)^2 \ll 4\lambda \tilde{R}_n = 16(N_s(\Delta_x^s)^2 + \bar{N}_r(\Delta_x^r)^2 + 2\sqrt{N_s \bar{N}_r}\Delta_x^s \Delta_x^r). \quad (22)$$

Note that this inequality always holds since $16N_s \gg 1$ and $16\bar{N}_r \gg 1$, which proves the feasibility of the proposed channel model for TP HMIMOS comunication systems.

IV. Interference Elimination in TP MU-HMIMOS

There are mainly two interference sources in TP MU-HMIMOS systems: one from the cross-polarization and the other from the inter-user interference. Different from DP systems, the cross-polarization interference in TP systems is much more complicated, since it relates to the sum of two cross-polarization components. To eliminate these two interference sources, a precoding scheme based on user clustering is presented in this paper. However, this scheme compromises the system diversity. Thus, a two-layer precoding design is further presented to fully exploit diversity. Specifically, in the first layer, the interference from the cross-polarization components is eradicated by Gaussian elimination approach. In the second layer, the interference from other users in the co-polarized channels is suppressed through BD method. Here are details of two proposed precoding schemes.

A. User-Cluster-Based Precoding

Based on the proposed channel model $\mathbf{H}$ in (19), the input-output relationship of the considered TP HMIMOS comuunication system is given by

$$\mathbf{y} = \begin{bmatrix} \mathbf{H}_{xx} & \mathbf{H}_{xy} & \mathbf{H}_{xz} \\ \mathbf{H}_{yx} & \mathbf{H}_{yy} & \mathbf{H}_{yz} \\ \mathbf{H}_{zx} & \mathbf{H}_{zy} & \mathbf{H}_{zz} \end{bmatrix} \begin{bmatrix} \mathbf{x}_x \\ \mathbf{x}_y \\ \mathbf{x}_z \end{bmatrix} + \mathbf{n}, \quad (23)$$

where $\mathbf{x} = [\mathbf{x}_x^T, \mathbf{x}_y^T, \mathbf{x}_z^T]^T \in \mathbb{C}^{3N_r \times 1}$ with $\mathbf{x}_p \in \mathbb{C}^{N_r \times 1}, p \in \{x, y, z\}$ is the transmitted signal, $\mathbf{y} \in \mathbb{C}^{3N_r \times 1}$ is the received signal, and $\mathbf{n} \in \mathbb{C}^{3N_r \times 1}$ is the additive Gaussian noise.

Authorized licensed use limited to: Zhejiang University. Downloaded on December 14,2023 at 13:10:36 UTC from IEEE Xplore. Restrictions apply.

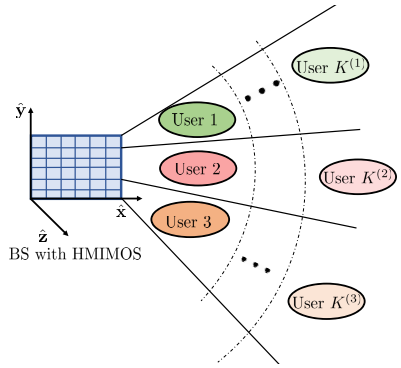

Fig. 3. User cluster scheme in TP MU-HMIMOS systems.

It can be observed that the received signal suffers from the interference caused by two cross-polarization components, which is more severe than the interference in DP systems. Therefore, in order to suppress the cross-polarization interference, the precoding matrices $\mathbf{P}_x, \mathbf{P}_y$, and $\mathbf{P}_z$ are introduced as follows:

$$\begin{aligned}\mathbf{y}^{(1)} &= \mathbf{H}_{xx}\mathbf{P}_x\mathbf{x}_x + \mathbf{H}_{xy}\mathbf{P}_y\mathbf{x}_y + \mathbf{H}_{xz}\mathbf{P}_z\mathbf{x}_z,\\ \mathbf{y}^{(2)} &= \mathbf{H}_{yx}\mathbf{P}_x\mathbf{x}_x + \mathbf{H}_{yy}\mathbf{P}_y\mathbf{x}_y + \mathbf{H}_{yz}\mathbf{P}_z\mathbf{x}_z,\\ \mathbf{y}^{(3)} &= \mathbf{H}_{zx}\mathbf{P}_x\mathbf{x}_x + \mathbf{H}_{zy}\mathbf{P}_y\mathbf{x}_y + \mathbf{H}_{zz}\mathbf{P}_z\mathbf{x}_z. \end{aligned} \tag{24}$$

Intuitively, the cross-polarization interference can be mitigated if each user is assigned to only one polarization. Inspired by this idea, a precoding design based on user clustering was proposed in [44] for DP communication systems. According to this scheme, each data stream can be independently transmitted in different polarizations without interference. This scheme can be also extended to TP systems, as shown in Fig. 3. Specifically, the K users are sorted in different polarizations based on their distances to the BS, such that $d_1 < d_2 < \ldots < d_K$, resulting in three disjoint subsets: *i*) the x-subset $\mathcal{L}^x = \{1, 4, \ldots, K^{(1)}\}$ containing $|\mathcal{L}^x| = K/3$ (we consider the case that $K/3$ is an integer) users with $K^{(1)} = K/3 - 2$; *ii*) the y-subset $\mathcal{L}^y = \{2, 5, \ldots, K^{(2)}\}$ with $|\mathcal{L}^y| = K/3$ users where $K^{(2)} = K/3 - 1$; and *iii*) the z-subset $\mathcal{L}^z = \{3, 6, \ldots, K^{(3)}\}$ including $|\mathcal{L}^z| = K/3$ users with $K^{(3)} = K/3$. The corresponding sub-channel matrices for the user cluster are derived as:

$$\tilde{\mathbf{H}}_x^{\mathrm{UC}} = \begin{bmatrix} h_{11}^{(1)} \ldots h_{1N_s}^{(1)} \\ h_{11}^{(4)} \ldots h_{1N_s}^{(4)} \\ \ddots \\ h_{\bar{N}_r 1}^{K^{(1)}} \ldots h_{\bar{N}_r N_s}^{K^{(1)}} \end{bmatrix}, \quad \tilde{\mathbf{H}}_y^{\mathrm{UC}} = \begin{bmatrix} h_{11}^{(2)} \ldots h_{1N_s}^{(2)} \\ h_{11}^{(5)} \ldots h_{1N_s}^{(5)} \\ \ddots \\ \tilde{h}_{\bar{N}_r 1}^{K^{(2)}} \ldots h_{\bar{N}_r N_s}^{K^{(2)}} \end{bmatrix},$$

$$\tilde{\mathbf{H}}_z^{\mathrm{UC}} = \begin{bmatrix} h_{11}^{(3)} \ldots h_{1N_s}^{(3)} \\ h_{11}^{(6)} \ldots h_{1N_s}^{(6)} \\ \ddots \\ h_{\bar{N}_r 1}^{K^{(3)}} \ldots h_{\bar{N}_r N_s}^{K^{(3)}} \end{bmatrix} \in \mathbb{C}^{K\bar{N}_r/3 \times N_s}. \tag{25}$$

Since each user is assigned to one polarization, the cross-polarization and inter-user interference terms are suppressed. The corresponding precoding matrices for three polarizations are designed as follows $\forall i = 1, 2, \ldots, \bar{N}_r$:

$$\begin{aligned}\mathbf{P}_q &= [p_{q,1}^{(1)}, \ldots, p_{q,\bar{N}_r}^{(1)}; \ldots; p_{q,1}^{(K)}, \ldots, p_{q,\bar{N}_r}^{(K)}],\\ q \in \{x, y, z\}, &\begin{cases} p_{q,i}^{(k)} = 1, & k \in \mathcal{L}^q \\ p_{q,i}^{(k)} = 0, & \text{otherwise.} \end{cases}\end{aligned} \tag{26}$$

However, the proposed user-cluster-based precoding scheme mitigates cross-polarization interference at the cost of impacting system diversity. In fact, the system diversity is reduced, since there is only one third of the patch antennas used for each user. Therefore, in order to fully exploit the polarization diversity, we next present a two-layer precoding scheme.

B. Two-Layer Precoding

1) First-Layer Precoding (Gaussian Elimination Based Precoding): Different from DP systems, the interference is much more complex since it involves the sum of two cross-polarization components in TP systems. In order to eliminate the cross-polarization interference sum, a Gaussian elimination based precoding design is introduced. Specifically, the precoding matrices $\mathbf{P}_x, \mathbf{P}_y$ and $\mathbf{P}_z$ force the interference of two cross-polarization components in all received signals to be zero, i.e.,

$$\mathbf{H}^{\mathrm{XP}}\mathbf{P} = \begin{bmatrix} \mathbf{0} & \mathbf{H}_{xy} & \mathbf{H}_{xz} \\ \mathbf{H}_{yx} & \mathbf{0} & \mathbf{H}_{yz} \\ \mathbf{H}_{zx} & \mathbf{H}_{zy} & \mathbf{0} \end{bmatrix} \begin{bmatrix} \mathbf{P}_x \\ \mathbf{P}_y \\ \mathbf{P}_z \end{bmatrix} = \begin{bmatrix} \mathbf{0} \\ \mathbf{0} \\ \mathbf{0} \end{bmatrix}, \tag{27}$$

where $\mathbf{H}^{\mathrm{XP}}$ collects all cross-polarization components, and $\mathbf{P} = [\mathbf{P}_x^T, \mathbf{P}_y^T, \mathbf{P}_z^T]^T$. Thus, the matrix $\mathbf{P}$ lies in the null-space of the matrix $\mathbf{H}^{\mathrm{XP}}$.

Perform Gaussian elimination to the matrix $\mathbf{H}^{\mathrm{XP}}$ first, i.e.,

$$\begin{aligned}&\begin{bmatrix} \mathbf{0} & \mathbf{I}_{N_s} & \mathbf{H}_{xy}^{-1}\mathbf{H}_{xz} \\ \mathbf{H}_{yx} & \mathbf{0} & \mathbf{H}_{yz} \\ \mathbf{H}_{zx} & \mathbf{H}_{zy} & \mathbf{0} \end{bmatrix}\\ &= \begin{bmatrix} \mathbf{0} & \mathbf{I}_{N_s} & \mathbf{H}_{xy}^{-1}\mathbf{H}_{xz} \\ \mathbf{I}_{N_s} & \mathbf{0} & \mathbf{H}_{yx}^{-1}\mathbf{H}_{yz} \\ \mathbf{0} & \mathbf{0} & -\left(\mathbf{H}_{zx}^{-1}\mathbf{H}_{zy}\right)^{-1}\mathbf{H}_{yx}^{-1}\mathbf{H}_{yz} - \mathbf{H}_{xy}^{-1}\mathbf{H}_{xz} \end{bmatrix}. \end{aligned} \tag{28}$$

Let

$$\begin{bmatrix} \mathbf{0} & \mathbf{I}_{N_s} & \bar{\mathbf{A}} \\ \mathbf{I}_{N_s} & \mathbf{0} & \bar{\mathbf{B}} \\ \mathbf{0} & \mathbf{0} & \bar{\mathbf{C}} \end{bmatrix} \begin{bmatrix} \mathbf{P}_x \\ \mathbf{P}_y \\ \mathbf{P}_z \end{bmatrix} = \begin{bmatrix} \mathbf{0} \\ \mathbf{0} \\ \mathbf{0} \end{bmatrix}, \tag{29}$$

where

$$\begin{aligned}&\bar{\mathbf{A}} = \mathbf{H}_{xy}^{-1}\mathbf{H}_{xz}, \quad \bar{\mathbf{B}} = \mathbf{H}_{yx}^{-1}\mathbf{H}_{yz},\\ &\bar{\mathbf{C}} = -\left(\mathbf{H}_{zx}^{-1}\mathbf{H}_{zy}\right)^{-1}\mathbf{H}_{yx}^{-1}\mathbf{H}_{yz} - \mathbf{H}_{xy}^{-1}\mathbf{H}_{xz}. \end{aligned} \tag{30}$$

Thus,

$$\mathbf{P}_y = -\bar{\mathbf{A}}\mathbf{P}_z, \mathbf{P}_x = -\bar{\mathbf{B}}\mathbf{P}_z, \tag{31}$$

where $\mathbf{P}_z$ lies in the null space of $\bar{\mathbf{C}}$, i.e., $\bar{\mathbf{C}}\mathbf{0}$. To compute the $\mathbf{P}_z$, we adopt orthogonal projection operator [45], i.e.,

$$\bar{\mathbf{C}}^{\mathbf{0}} = \mathbf{I}_{N_s} - \bar{\mathbf{C}}^{\dagger}(\bar{\mathbf{C}}\bar{\mathbf{C}}^{\dagger})^{-1}\bar{\mathbf{C}}, \tag{32}$$

Authorized licensed use limited to: Zhejiang University. Downloaded on December 14,2023 at 13:10:36 UTC from IEEE Xplore. Restrictions apply.

and

$$\mathbf{P}_z = \mathbf{H}_{zz}^{\dagger}\left(\mathbf{H}_{zz}\bar{\mathbf{C}}^{\mathbf{0}}\mathbf{H}_{zz}^{\dagger}\right)^{-1}\mathbf{H}_{zz}\bar{\mathbf{C}}^{\mathbf{0}}. \tag{33}$$

With the designed precoding matrix $\mathbf{P}$, the channels are

$$\begin{aligned}
&\mathbf{H}_{xx}\mathbf{P}_x + \mathbf{H}_{xy}\mathbf{P}_y + \mathbf{H}_{xz}\mathbf{P}_z \\
&\quad = -\mathbf{H}_{xx}\mathbf{H}_{yx}^{-1}\mathbf{H}_{yz}\mathbf{P}_z - \mathbf{H}_{xy}\mathbf{H}_{xy}^{-1}\mathbf{H}_{xz}\mathbf{P}_z + \mathbf{H}_{xz}\mathbf{P}_z \\
&\quad = -\mathbf{H}_{xx}\mathbf{H}_{yx}^{-1}\mathbf{H}_{yz}\mathbf{P}_z = \mathbf{H}_{xx}\mathbf{P}_x, \\
&\mathbf{H}_{yx}\mathbf{P}_x + \mathbf{H}_{yy}\mathbf{P}_y + \mathbf{H}_{yz}\mathbf{P}_z \\
&\quad = -\mathbf{H}_{yx}\mathbf{H}_{yx}^{-1}\mathbf{H}_{yz}\mathbf{P}_z - \mathbf{H}_{yy}\mathbf{H}_{xy}^{-1}\mathbf{H}_{xz}\mathbf{P}_z + \mathbf{H}_{yz}\mathbf{P}_z \\
&\quad = -\mathbf{H}_{yy}\mathbf{H}_{xy}^{-1}\mathbf{H}_{xz}\mathbf{P}_z = \mathbf{H}_{yy}\mathbf{P}_y.
\end{aligned} \tag{34}$$

Thus, the received signal with the precoded channel is

$$\begin{aligned}
\mathbf{y} &= \begin{bmatrix}\mathbf{y}_x\\ \mathbf{y}_y\\ \mathbf{y}_z\end{bmatrix} = \begin{bmatrix}\mathbf{H}_{xx} & \mathbf{H}_{xy} & \mathbf{H}_{xz}\\ \mathbf{H}_{yx} & \mathbf{H}_{yy} & \mathbf{H}_{yz}\\ \mathbf{H}_{zx} & \mathbf{H}_{zy} & \mathbf{H}_{zz}\end{bmatrix}\begin{bmatrix}\mathbf{P}_x\mathbf{x}_x\\ \mathbf{P}_y\mathbf{x}_y\\ \mathbf{P}_z\mathbf{x}_z\end{bmatrix} + \mathbf{n} \\
&= \begin{bmatrix}\mathbf{H}_{xx}^{\mathbf{P}} & \mathbf{0} & \mathbf{0}\\ \mathbf{0} & \mathbf{H}_{yy}^{\mathbf{P}} & \mathbf{0}\\ \mathbf{0} & \mathbf{0} & \mathbf{H}_{zz}^{\mathbf{P}}\end{bmatrix}\begin{bmatrix}\mathbf{x}_x\\ \mathbf{x}_y\\ \mathbf{x}_z\end{bmatrix},
\end{aligned} \tag{35}$$

where $\mathbf{H}_{qq}^{\mathbf{P}} = \mathbf{H}_{qq}\mathbf{P}_q, q \in \{x, y, z\}$ is the co-polarized channel in the first-layer precoding.

Through Gaussian elimination method, the cross-polarization interference is eliminated in the first-layer. Thus, we only need to further eliminate the inter-user interference in each co-polarized channel, which is performed in the second-layer precoding as discussed in the next subsection.

2) Second-Layer Precoding (BD Based Precoding): With the transmit polarization vector $\mathbf{F}_s^{(k)} \in \mathbb{C}^{3N_s \times N_s}$ and receive polarization vector $\mathbf{F}_r^{(k)} \in \mathbb{C}^{3\bar{N}_r \times \bar{N}_r}$, the precoded channel for the kth user becomes $(\mathbf{F}_r^{(k)})^T\mathbf{H}^{\mathbf{P}^{(k)}}\mathbf{F}_s^{(k)}$, where the co-polarized channel matrix $\mathbf{H}^{\mathbf{P}^{(k)}}$ is

$$\mathbf{H}^{\mathbf{P}^{(k)}} = \begin{bmatrix}\mathbf{H}_{xx}^{\mathbf{P}\ (k)} & \mathbf{0} & \mathbf{0}\\ \mathbf{0} & \mathbf{H}_{yy}^{\mathbf{P}\ (k)} & \mathbf{0}\\ \mathbf{0} & \mathbf{0} & \mathbf{H}_{zz}^{\mathbf{P}\ (k)}\end{bmatrix}. \tag{36}$$

Let $C_x = \mathrm{rank}(\mathbf{H}_{xx}^{\mathbf{P}}), C_y = \mathrm{rank}(\mathbf{H}_{yy}^{\mathbf{P}})$ and $C_z = \mathrm{rank}(\mathbf{H}_{zz}^{\mathbf{P}})$ be ranks of each co-polarization sub-channel, respectively. In typical scenarios, $C_x = C_y = C_z$, i.e., the number of independent channels in three polarizations is the same. However, zth polarization vanishes with the distance along z-axis, thus, practically, $C_z \neq C_x, C_y$ in TP systems.

Perform BD in each co-polarized channel to design the precoding matrix $\mathbf{F}$. Taking $\mathbf{H}_{xx}^{\mathbf{P}}$ as an example, we have

$$\mathbf{y}_{xx} = \mathbf{H}_{xx}^{\mathbf{P}}\mathbf{F}_{xx}\mathbf{x}_{xx} + \mathbf{n}_{xx} \in \mathbb{C}^{N_r \times 1}, \tag{37}$$

and the kth user is

$$\mathbf{y}_{xx}^{(k)} = \mathbf{H}_{xx}^{\mathbf{P}\ (k)}\mathbf{F}_{xx}^{(k)}\mathbf{x}_{xx}^{(k)} + \mathbf{H}_{xx}^{\mathbf{P}\ (k)}\sum_{k' \neq k}^{K}\mathbf{F}_{xx}^{(k')}\mathbf{x}_{xx}^{(k')} + \mathbf{n}_{xx}^{(k)}. \tag{38}$$

The interference channel matrix for the kth user is

$$\begin{aligned}
\bar{\mathbf{T}}_{xx}^{(k)} = \big[&(\mathbf{H}_{xx}^{\mathbf{P}\ (1)})^T, \ldots, (\mathbf{H}_{xx}^{\mathbf{P}\ (k-1)})^T, \\
&\times(\mathbf{H}_{xx}^{\mathbf{P}\ (k+1)})^T, \ldots, (\mathbf{H}_{xx}^{\mathbf{P}\ (K)})^T\big]^T.
\end{aligned} \tag{39}$$

Perform singular value decomposition (SVD) decomposition of $\bar{\mathbf{T}}_{xx}^{(k)}$,

$$\bar{\mathbf{T}}_{xx}^{(k)} = \bar{\mathbf{U}}_{\bar{T}}^{(k)}\begin{bmatrix}\bar{\mathbf{\Lambda}}_{\mathbf{T}}^{(k)} & \mathbf{0} =\\ \mathbf{0} & \mathbf{0}\end{bmatrix}\begin{bmatrix}\bar{\mathbf{V}}_{\bar{T},\mathbf{1}}^{(k)}\\ \bar{\mathbf{V}}_{\bar{T},\mathbf{0}}^{(k)}\end{bmatrix}. \tag{40}$$

Therefore,

$$\dot{\mathbf{H}}_{xx}^{(k)} = \mathbf{H}_{xx}^{\mathbf{P}\ (k)}\bar{\mathbf{V}}_{\mathbf{T},\mathbf{0}}^{(k)} \in \mathbb{C}^{\bar{N}_r \times \left(N_s - \mathrm{rank}(\bar{\mathbf{T}}^{(k)})\right)}, \tag{41}$$

where the projection on the null space $\bar{\mathbf{V}}_{\mathbf{T},\mathbf{0}}^{(k)}$ enables inter-user interference elimination.

The SVD decomposition of the channel $\dot{\mathbf{H}}^{(k)}$ is

$$\dot{\mathbf{H}}_{xx}^{(k)} = \dot{\mathbf{U}}^{(k)}\begin{bmatrix}\dot{\mathbf{\Lambda}}^{(k)} & \mathbf{0}\\ \mathbf{0} & \mathbf{0}\end{bmatrix}\begin{bmatrix}\dot{\mathbf{V}}_{\mathbf{1}}^{(k)}]\\ \dot{\mathbf{V}}_{\mathbf{0}}^{(k)}\end{bmatrix}. \tag{42}$$

The precoding matrix is

$$\mathbf{F}_{xx} = [\bar{\mathbf{V}}_{\mathbf{T},\mathbf{0}}^{(1)}\dot{\mathbf{V}}_{\mathbf{1}}^{(1)}, \ldots, \bar{\mathbf{V}}_{\mathbf{T},\mathbf{0}}^{(K)}\dot{\mathbf{V}}_{\mathbf{1}}^{(K)}] \in \mathbb{C}^{\bar{N}_s \times \bar{N}_r}, \tag{43}$$

where the inter-user interference is removed and the user signal is strengthened at the same time.

The similar design can be applied to $\mathbf{H}_{yy}^{\mathbf{P}}$ and $\mathbf{H}_{zz}^{\mathbf{P}}$ to obtain $\mathbf{F}_{yy}$ and $\mathbf{F}_{zz}$. The spatially precoded channel is

$$\mathbf{H}^{\mathbf{F}} = \begin{bmatrix}\mathbf{H}_{xx}^{\mathbf{F}} & \mathbf{0} & \mathbf{0}\\ \mathbf{0} & \mathbf{H}_{yy}^{\mathbf{F}} & \mathbf{0}\\ \mathbf{0} & \mathbf{0} & \mathbf{H}_{zz}^{\mathbf{F}}\end{bmatrix} \in \mathbb{C}^{3N_r \times 3N_r}, \tag{44}$$

where the channel $\mathbf{H}_{pq}^{\mathbf{F}} = \mathbf{H}_{pq}^{\mathbf{P}}\mathbf{F}_{pq}$, $p, q \in \{x, y, z\}$.

We have the received signal

$$\mathbf{y} = \mathbf{H}^{\mathbf{F}}\mathbf{x} = \begin{bmatrix}\mathbf{H}_{xx}^{\mathbf{F}} & \mathbf{0} & \mathbf{0}\\ \mathbf{0} & \mathbf{H}_{yy}^{\mathbf{F}} & \mathbf{0}\\ \mathbf{0} & \mathbf{0} & \mathbf{H}_{zz}^{\mathbf{F}}\end{bmatrix}\begin{bmatrix}\mathbf{x}_x\\ \mathbf{x}_y\\ \mathbf{x}_z\end{bmatrix} \in \mathbb{C}^{3N_r \times 1}. \tag{45}$$

Therefore, through the BD elimination method in the second-layer precoding, the inter-user interference in three co-polarized channels is removed. It should be noted, however, that although the proposed two-layer precoding scheme removes the cross-polarization interference without sacrificing polarization diversity, it requires higher computational complexity compared with the user-cluster-based precoding. As previoously mentioned in this section, the ranks of three co-polarized channels are different in TP systems, thus, an efficient PA is necessary. This is explicitly discussed in the following section.

V. Power Allocation in TP Systems

Since the ranks of three independent channels $\mathbf{H}_{pp}^{\mathbf{F}}, p \in \{x, y, z\}$ are different, i.e., the power imbalance exists, an effective PA becomes important. There are mainly three PA schemes in TP system.

- **PA1 (Polarization Selection based Power Allocation):** In PA1, one of three polarizations with the best channel condition is selected for data transmission, then the users in the selected polarization are allocated power using water filling method.

  It should be noted that PA1 can also be further refined, i.e., the polarized channel for each user is selected, and then all selected channels are rearranged for further PA

Authorized licensed use limited to: Zhejiang University. Downloaded on December 14,2023 at 13:10:36 UTC from IEEE Xplore. Restrictions apply.

among users. This is recommended when some users are far away from the transmitter, because the zth polarized component decays fast and only x, yth polarized components dominate the communications. However, the complexity of this scheme is heavily high, thus we do not apply it in this work.

- **PA2 (Equal Power Allocation):** In PA2, three polarizations are allocated with the same power, and then users in each polarizations are allocated equal power.

A simplified comparison between PA1 and PA2 is given here, the power allocated to the pth polarization is Q_p, and the power allocated to the kth user in the pth polarization is $G_{k,p}$. Therefore, in PA1, $Q_p = 1$ and $G_{k,p}$ are obtained using water filling PA method. In PA2, $Q_p = \frac{1}{3}$ and $G_{k,p} = \frac{1}{N_r}$. For fair comparison, we assume that all polarized channels are normalized and only focus on PA among three polarizations. Accordingly, the capacity of PA1 and PA2 are

$$\mathcal{R}^{\mathrm{PA1}} = \log_2\left(1 + \frac{Q_p}{\sigma_w^2}\right), \quad \mathcal{R}^{\mathrm{PA2}} = 3\log_2\left(1 + \frac{Q_p}{3\sigma_w^2}\right). \tag{46}$$

Since

$$\left(1 + \frac{Q_p}{3\sigma_w^2}\right)^3 = \frac{Q_p^3}{27\sigma_w^6} + \frac{Q_p^2}{3\sigma_w^4} + \frac{Q_p}{\sigma_w^2} + 1, \tag{47}$$

we have

$$\mathcal{R}^{\mathrm{PA1}} < \mathcal{R}^{\mathrm{PA2}}, \tag{48}$$

which substantiates that three polarizations should all be employed instead of just selecting the best polarized channel for data transmission. Based upon this observation, we propose a two-layer PA method to fully exploit three polarized channels, which is termed as **PA3** in this paper. Specifically, in the first layer, the three polarizations are allocated different power weights. Then, the users in the same polarization is allocated power using water filling method. Therefore, the power allocated to users in different polarizations is the product of the power in the first layer and second layer. In the following subsections, the two-layer PA scheme, i.e., PA3, is illustrated.

A. The First Layer of PA3: PA Among Different Polarizations

Typically, waves in three polarizations experience different pathloss. Intuitively, the polarization state with the highest power is the best link for communications. Thus, it is necessary to allocate power based on polarization state. Here, we define a polarized matrix

$$\check{\mathbf{E}} = \begin{bmatrix} \check{E}_{xx} & 0 & 0 \\ 0 & \check{E}_{yy} & 0 \\ 0 & 0 & \check{E}_{zz} \end{bmatrix} = \begin{bmatrix} |\mathbf{H}^{\mathbf{F}}_{xx}|_f^2 & 0 & 0 \\ 0 & |\mathbf{H}^{\mathbf{F}}_{yy}|_f^2 & 0 \\ 0 & 0 & |\mathbf{H}^{\mathbf{F}}_{zz}|_f^2 \end{bmatrix}, \tag{49}$$

where $|\mathbf{H}^{\mathbf{F}}|_f^2$ is the squared Frobenius norm of the matrix $\mathbf{H}^{\mathbf{F}}$.

The water filling based PA is applied to the defined polarized matrix $\check{\mathbf{E}}$, i.e., the power allocated to the pth polarization is $Q_p = (\epsilon - \frac{\sigma_w^2}{\check{E}_{pp}})^+$ [46].

B. The Second Layer of PA3: PA Among Different Users in the Same Polarization

In the first-layer precoding,

$$\mathbf{H}_{xx}^{\mathbf{F}\ (k)} = \tilde{\mathbf{U}}^{(k)} \begin{bmatrix} \tilde{\mathbf{\Lambda}}^{(k)} & \mathbf{0} \\ \mathbf{0} & \mathbf{0} \end{bmatrix} \tilde{\mathbf{V}}^{(k)}, \tag{50}$$

where $\tilde{\mathbf{\Lambda}}^{(k)} = \mathrm{diag}(\tilde{\lambda}_{k,1}, \ldots, \tilde{\lambda}_{k,r_k})$, and $r_k = \mathrm{rank}(\mathbf{H}_{xx}^{\mathbf{F}\ (k)})$. We have the block diagonal matrix for all K users, i.e.,

$$\tilde{\mathbf{\Lambda}} = \mathrm{blkdiag}[\tilde{\mathbf{\Lambda}}^{(1)}, \ldots, \tilde{\mathbf{\Lambda}}^{(K)}]. \tag{51}$$

Since

$$\begin{aligned} &\mathbf{H}_{xx}^{\mathbf{F}\ (k)} \mathbf{G}_{xx}^{(k)} [\mathbf{G}_{xx}^{(k)}]^\dagger [\mathbf{H}_{xx}^{\mathbf{F}\ (k)}]^\dagger \\ &\quad = \tilde{\mathbf{U}}^{(k)} \begin{bmatrix} \tilde{\mathbf{\Lambda}}^{(k)} & \mathbf{0} \\ \mathbf{0} & \mathbf{0} \end{bmatrix} \tilde{\mathbf{G}}_{xx}^{(k)} \begin{bmatrix} [\tilde{\mathbf{\Lambda}}^{(k)}]^\dagger & \mathbf{0} \\ \mathbf{0} & \mathbf{0} \end{bmatrix} [\tilde{\mathbf{U}}^{(k)}]^\dagger, \end{aligned} \tag{52}$$

where $\mathbf{G}_{xx}^{(k)}$ is the power allocated to the kth user in xth polarization, and $\tilde{\mathbf{G}}_{xx}^{(k)} = \tilde{\mathbf{V}}^{(k)} \mathbf{G}_{xx}^{(k)} [\mathbf{G}_{xx}^{(k)}]^\dagger [\tilde{\mathbf{V}}^{(k)}]^\dagger$.

The water filling is performed on the diagonal elements of $\tilde{\mathbf{\Lambda}}$ to determine the optimal power matrix $\mathbf{G}$. Specifically, for the ith element in the kth diagonal power matrix for the kth user, the power is $G_{k,i} = (\epsilon - \frac{\sigma_w^2}{|\lambda_{k,i}|^2})^+$ [46], [47], [48], where $\tilde{\lambda}_{k,i}$ is the ith element in the kth diagonal block in $\tilde{\mathbf{\Lambda}}$.

Therefore, combining the allocated power in two layers for the kth user in pth polarization as $Q_p G_{k,i}$ (or $Q_p G_k$), we have the PA matrix $(\mathbf{Q} \otimes \mathbf{I}_{KN_r})\mathbf{G}$, where $\mathbf{Q}$ and $\mathbf{G}$ are diagonal matrices.

VI. Performance Evaluation

In this section, we provide the theoretical analysis and simulation evaluation of the channel model, i.e., channel correlation factors and DoF. In addition, the sum rate of the proposed two precoding schemes are also evaluated.

A. Channel Correlation Analysis

There are mainly two channel correlation matrices: the correlation matrix $\mathbf{R}^s$ at the transmitter and the correlation matrix $\mathbf{R}^r$ at each receiver. The nth transmit patch antenna with location $\mathbf{r}_n$, and the ℓth transmit patch antenna with location $\mathbf{r}_\ell$, will be spatially correlated by the following factor:

$$\begin{aligned} \mathbf{R}^s(\mathbf{r}'_n, \mathbf{r}'_\ell) &\propto \left\langle \mathbf{E}(\mathbf{r}'_n) \mathbf{E}^\dagger(\mathbf{r}'_\ell) \right\rangle \\ &= \int\int d^2\mathbf{r}_m d^2\mathbf{r}_{m'} \bar{\mathbf{G}}(\mathbf{r}_m, \mathbf{r}'_n) \\ &\quad \times \bar{\mathbf{G}}^\dagger(\mathbf{r}_{m'}, \mathbf{r}'_\ell) \left\langle \mathbf{J}(\mathbf{r}_m) \mathbf{J}(\mathbf{r}_{m'}) \right\rangle, \end{aligned} \tag{53}$$

where $\dagger$ denotes transpose operation. Due to the reciprocity, the receive correlation can also be obtained in the same way. We assume that $\langle \mathbf{J}(\mathbf{r}_m)\mathbf{J}(\mathbf{r}_{m'})\rangle = \delta_{mm'}/3$, as a consequence of the fluctuation-dissipation theorem [49], [50], we have:

$$\mathbf{R}^s(\mathbf{r}'_n, \mathbf{r}'_\ell) \propto \mathrm{Im}\{\bar{\mathbf{G}}_c(d_{n\ell})\}, \tag{54}$$

where $d_{n\ell}$ is the distance between the nth and ℓth transmit patch antennas, and $\bar{\mathbf{G}}_c(d_{n\ell})$ is the dyadic Green function for a bounded surface.

Inspired by the theory of images for bounded planes, the dyadic Green function $\bar{\mathbf{G}}_c(d_{n\ell})$ is the superposition of the

Authorized licensed use limited to: Zhejiang University. Downloaded on December 14,2023 at 13:10:36 UTC from IEEE Xplore. Restrictions apply.

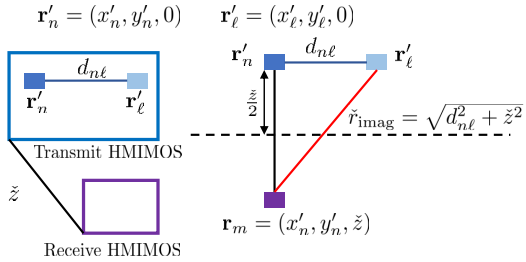

Fig. 4. Free space with the original source $\mathbf{r}'_n = (x'_n, y'_n, 0)$ and its image $\mathbf{r}_m = (x'_n, y'_n, \check{z})$.

electric free-space dyadic Green functions [51]. As shown in Fig. 4, the source point $\mathbf{r}'_n = (x'_n, y'_n, 0)$ has an image point $\mathbf{r}_m = (x'_n, y'_n, \check{z})$, and the field point (also in transmit HMIMOS) is $\mathbf{r}'_\ell = (x'_\ell, y'_\ell, 0)$. Therefore, $\bar{\mathbf{G}}_c(d_{n\ell})$ is the sum of free space Green function $\bar{\mathbf{G}}_0(\mathbf{r}'_n, \mathbf{r}'_\ell)$ induced by original source point $\mathbf{r}'_n$ and Green function $\bar{\mathbf{G}}_{\text{imag}}(\mathbf{r}_m, \mathbf{r}'_\ell)$ due to the image source $\mathbf{r}_m$, which is given by:

$$\bar{\mathbf{G}}_c(\mathbf{r}'_n, \mathbf{r}'_\ell) = \bar{\mathbf{G}}_0(\mathbf{r}'_n, \mathbf{r}'_\ell) + \bar{\mathbf{G}}_{\text{imag}}(\mathbf{r}_m, \mathbf{r}'_\ell), \tag{55}$$

where the free space Green function due to the nth transmit patch antenna is [51]

$$\bar{\mathbf{G}}_0(\mathbf{r}'_n, \mathbf{r}'_\ell) = \left[(\hat{x}\hat{x} + \hat{y}\hat{y} + \hat{z}\hat{z}) + \frac{1}{k^2}\nabla\left(\hat{x}\frac{\partial}{\partial x} + \hat{y}\frac{\partial}{\partial y} + \hat{z}\frac{\partial}{\partial z}\right)\right] g\left(\mathbf{r}'_n, \mathbf{r}'_\ell\right), \tag{56}$$

and the Green function of the image dyadic source $\mathbf{r}_m$ is [51]

$$\bar{\mathbf{G}}_{\text{imag}}(\mathbf{r}_m, \mathbf{r}'_\ell) = \left[(-\hat{x}\hat{x} - \hat{y}\hat{y} + \hat{z}\hat{z}) + \frac{1}{k^2}\nabla\left(-\hat{x}\frac{\partial}{\partial x} - \hat{y}\frac{\partial}{\partial y} + \hat{z}\frac{\partial}{\partial z}\right)\right] g(\mathbf{r}_m, \mathbf{r}'_\ell). \tag{57}$$

Since $\mathbf{r}_{\text{imag}} = \mathbf{r}_m - \mathbf{r}'_\ell = (x'_n - x'_\ell, y'_n - y'_\ell, \check{z}) = (\check{x}, \check{y}, \check{z})$, where $\check{x} = x'_n - x'_\ell, \check{y} = y'_n - y'_\ell$ are differences between the nth and ℓth transmit patch antennas, and $\check{z}$ is the distance between transmit and receive HMIMOS. The derivative of scalar Green function $g\left(\mathbf{r}_m, \mathbf{r}'_\ell\right)$ given in (8) is:

$$\check{g}_r = \frac{\partial g\left(\check{r}_{\text{imag}}\right)}{\partial \check{r}_{\text{imag}}} = \frac{ik_0\check{r}_{\text{imag}} - 1}{4\pi\check{r}_{\text{imag}}^2} e^{ik_0\check{r}_{\text{imag}}}, \tag{58}$$

where $\check{r}_{\text{imag}} = |\mathbf{r}_{\text{imag}}| = \sqrt{\check{x}^2 + \check{y}^2 + \check{z}^2}$, and $\frac{\partial}{\partial x}\check{r}_{\text{imag}} = -\frac{\check{x}}{\check{r}_{\text{imag}}}$. Therefore,

$$\frac{\partial}{\partial x} g\left(\check{r}_{\text{imag}}\right) = -\frac{\check{x}}{\check{r}_{\text{imag}}}\check{g}_r = -\frac{ik_0\check{r}_{\text{imag}} - 1}{4\pi\check{r}_{\text{imag}}^3}\check{x}e^{ik_0\check{r}_{\text{imag}}}. \tag{59}$$

Let $\check{f}_r = \frac{\check{g}_r}{\check{r}_{\text{imag}}}$, we have

$$\frac{\partial}{\partial \check{r}_{\text{imag}}}\check{f}_r = \frac{-k_0^2\check{r}_{\text{imag}}^2 - i3\ k_0\check{r}_{\text{imag}} + 3}{4\pi\check{r}_{\text{imag}}^4} e^{ik_0\check{r}_{\text{imag}}}. \tag{60}$$

We obtain the intermediate variable

$$\begin{aligned}\mathcal{G}_{xx}(\check{r}_{\text{imag}}) &= \frac{\partial}{\partial x}\left[\frac{\partial}{\partial x} g\left(\check{r}_{\text{imag}}\right)\right] = \frac{\partial}{\partial x}\left[\frac{\partial}{\partial x}\left(-\check{x}\check{f}_r\right)\right] \\ &= \left[\frac{ik_0\check{r}_{\text{imag}} - 1 + k_0^2\check{x}^2}{4\pi\check{r}_{\text{imag}}^3} + \frac{i3k_0\check{x}^2}{4\pi\check{r}_{\text{imag}}^4} - \frac{3\check{x}^2}{4\pi\check{r}_{\text{imag}}^5}\right] e^{ik_0\check{r}_{\text{imag}}}.\end{aligned} \tag{61}$$

Thus,

$$\left[\bar{\mathbf{G}}_{\text{imag}}(\mathbf{r}_m, \mathbf{r}'_\ell)\right]_{xx} = -g(\check{r}_{\text{imag}}) - \frac{1}{k_0^2}\mathcal{G}_{xx}(\check{r}_{\text{imag}}). \tag{62}$$

The imaginary part of $\left[\bar{\mathbf{G}}_{\text{imag}}(\mathbf{r}_m, \mathbf{r}'_\ell)\right]_{xx}$ is

$$\begin{aligned}&\text{Im}\left\{\left[\bar{\mathbf{G}}_{\text{imag}}(\check{r}_{\text{imag}})\right]_{xx}\right\} \\ &= -\frac{\sin(k_0\check{r}_{\text{imag}})}{4\pi\check{r}_{\text{imag}}} - \frac{\cos(k_0\check{r}_{\text{imag}})}{4\pi k_0\check{r}_{\text{imag}}^2} + \frac{\sin(k_0\check{r}_{\text{imag}})}{4\pi k_0^2\check{r}_{\text{imag}}^3} \\ &\quad - \frac{\check{x}^2\sin(k_0\check{r}_{\text{imag}})}{4\pi\check{r}_{\text{imag}}^3} - \frac{3\check{x}^2\cos(k_0\check{r}_{\text{imag}})}{4\pi k_0\check{r}_{\text{imag}}^4} \\ &\quad + \frac{3\check{x}^2\sin(k_0\check{r}_{\text{imag}})}{4\pi k_0^2\check{r}_{\text{imag}}^5}.\end{aligned} \tag{63}$$

Similarly, the imaginary part of the xth polarization in $\bar{\mathbf{G}}_0(\mathbf{r}'_n, \mathbf{r}'_\ell)$ is given by:

$$\begin{aligned}\text{Im}\{\left[\bar{\mathbf{G}}_0(d_{n\ell})\right]_x\} &= \frac{\sin(k_0 d_{n\ell})}{4\pi d_{n\ell}} + \frac{\cos(k_0 d_{n\ell})}{4\pi k_0 d_{n\ell}^2} - \frac{\sin(k_0 d_{n\ell})}{4\pi k_0^2 d_{n\ell}^3} \\ &\quad - \frac{\check{x}^2\sin(k_0 d_{n\ell})}{4\pi d_{n\ell}^3} - \frac{3\check{x}^2\cos(k_0 d_{n\ell})}{4\pi k_0 d_{n\ell}^4} \\ &\quad + \frac{3\check{x}^2\sin(k_0 d_{n\ell})}{4\pi k_0^2 d_{n\ell}^5}.\end{aligned} \tag{64}$$

Therefore, the imaginary part of the xth co-polarization component of $\bar{\mathbf{G}}_c(\mathbf{r}'_n, \mathbf{r}'_\ell)$ is

$$\begin{aligned}\text{Im}\left\{\left[\bar{\mathbf{G}}_c(\mathbf{r}'_n, \mathbf{r}'_\ell)\right]_{xx}\right\} &= \text{Im}\left\{\left[\bar{\mathbf{G}}_0(d_{nn'})\right]_{xx}\right\} \\ &\quad + \text{Im}\left\{\left[\bar{\mathbf{G}}_{\text{imag}}(\check{r}_{\text{imag}})\right]_{xx}\right\},\end{aligned} \tag{65}$$

where the two summation terms are given in (63) and (64), respectively.

The above equations provide theoretical analysis for HMIMOS in NF regime. It is shown that both the spacing $d_{n\ell}$ and distance $\check{z}$ contribute to correlation factor. A similar derivation can be applied to the receiver correlation matrix $\mathbf{R}^r$. It should be noted that the user correlation is not considered in this subsection, however, a similar analysis is straightforward.

The role of the transmit patch antennas spacing on the transmit correlation factor $\mathbf{R}^s\left(\mathbf{r}'_n, \mathbf{r}'_\ell\right)$ as a function of the number of transmit antennas is illustrated in Fig. 5; the transmit correlation factor was computed via (54) and (65). The wavelength $\lambda = 1$ m, the transmitter is equipped with $N_s = 50$ patch antennas, and the distance between transmit and receive HMIMOS is $\check{z} = 0.3\lambda$. The spacing of adjacent transmit patch antennas is $\Delta_x^s = \Delta_y^s = 0.05\lambda, 0.2\lambda$ and 0.4λ, respectively. It can be observed from the figure that, the larger number of transmit antennas and the larger spacing between patch

Authorized licensed use limited to: Zhejiang University. Downloaded on December 14,2023 at 13:10:36 UTC from IEEE Xplore. Restrictions apply.

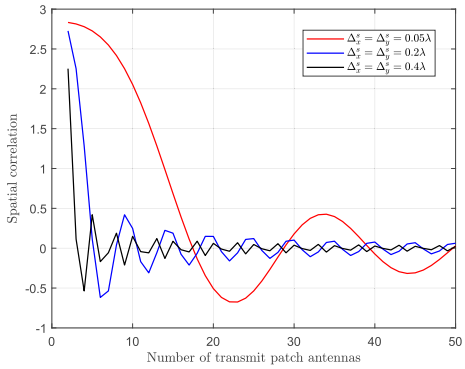

Fig. 5. Simulated spatial correlation factors for different transmit patch antennas spacing versus the number of transmit antennas with distance $\check{z} = 0.3\lambda$.

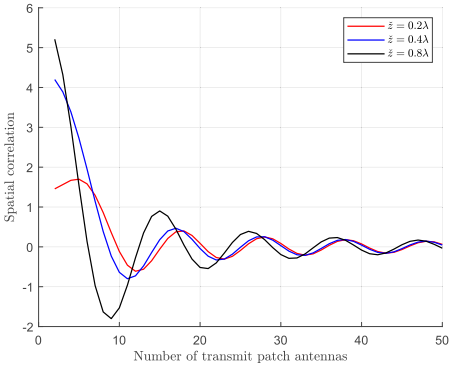

Fig. 6. Simulated spatial correlation factors for different distances between transmit and receive HMIMOS versus the number of transmit antennas with spacing $\Delta_x^s = \Delta_y^s = 0.1\lambda$.

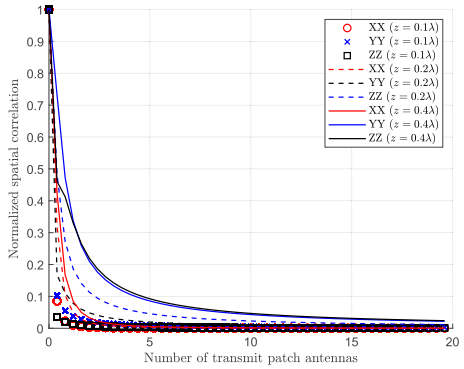

Fig. 7. Simulated normalized spatial correlation factors of all co-polarized channels for different users at distance z v.s. the number of transmit antennas.

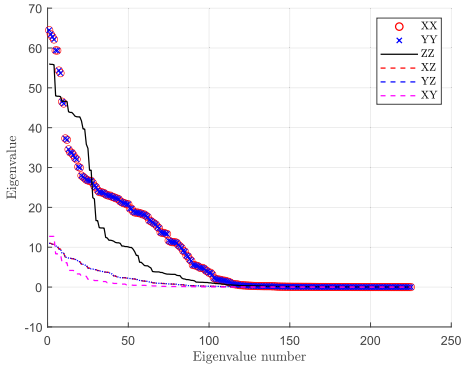

Fig. 8. Eigenvalues of the co-polarized and cross-polarized HMIMOS wireless channels for a single user lying in the NF regime ($z = \lambda$).

antennas reduce the normalized spatial correlation, since the distance between transmit patch antennas in (65) increases.

The distance $\check{z}$ between the transmit and receive HMIMOS also has impacts on transmit correlation factors, which is shown in Fig. 6. The wavelength $\lambda = 1$ m, the transmitter is equipped with $N_s = 50$ patch antennas with spacing $\Delta_x^s = \Delta_y^s = 0.1\lambda$, and the spacing of between two HMIMOS is $\check{z} = 0.2\lambda, 0.4\lambda$ and 0.8λ, respectively. An interesting observation is shown in Fig. 6, where it is demonstrated that users located further from the transmit HMIMOS experience higher spatial correlation, while those being closer to transmitter have smaller spatial correlation. From a first glance, it seems that this finding contradicts the conclusion in Fig. 5, where it is shown that the black curve $\check{z} = 0.8\lambda$ has 5 times higher correlation than the red curve $\check{z} = 0.2\lambda$ for the first two transmit patch antennas. However, the behavior in Fig. 6 is explained from the NF consideration. In this region, the EM field is quasi-static and spatial coherence occurs in the overlapped source areas of the order of πz^2 [49]. This implies that the users being placed with larger distance $\check{z}$ have a higher spatial coherence. Concluding, for fixed spacings and numbers of transmit patch antennas in the NF regime, the furthest user experiences the highest transmit spatial correlation.

The normalized correlation factors of all co-polarized channels are also given in Fig. 7. The wavelength is $\lambda = 1$ m, the transmitter is equipped with $N_s = 50$ patch antennas with spacing $\Delta_x^s = \Delta_y^s = 0.4\lambda$. Three users are placed at distance $z = 0.1\lambda, 0.2\lambda$ and 0.4λ, respectively. From the figure, all co-polarized channels of users at further distance suffer the higher correlation, which proves that the closer users are less spatially correlated in NF region. It can be observed from the figure that zth co-polarized channel has a higher spatial correlation factor than both xth and yth co-polarized channel, and its correlation decays fast with the number of transmit antennas, this can be accounted to that zth component dominates in the NF region and are more likely to be influenced by the spacing of two transmit patch antennas. On the other hand, the users at further distance z are more spatially correlated due to that the spatial coherence is proportionally to the area dependent of z, which exactly matches the former correlation analysis. What's more, the discrepancy of correlation factors in three polarization channels increases as the distance further, which motivates distance-aware procession in wireless communications.

The eigenvalues of co-/cross-polarized channels $\mathbf{R}^{ij} = [\mathbf{H}^{ij}]^\dagger \mathbf{H}^{ij}, i, j \in \{x, y, z\}$ are depicted in Fig. 8 and Fig. 9. The wavelength $\lambda = 1$ m, the transmitter and receiver are equipped with 225 patch antennas, and the spacing between patch antennas is 0.4λ. The user is located at distance $z = \lambda$ in Fig. 8 and $z = 3\lambda$ in Fig. 9. It can be observed from both figures that cross-polarized components are significant, thus, they need to be eliminated for efficient wireless communication. In addition, in short distance, non-zero eigenvalues of the zth co-polarized channel are as much as the other two co-polarized channels in Fig. 8, implying similar contributions to the xth and yth co-polarized channels in the system. However, as shown in Fig. 9, when distance becomes further, the xth and yth co-polarized channels are gradually more

Authorized licensed use limited to: Zhejiang University. Downloaded on December 14,2023 at 13:10:36 UTC from IEEE Xplore. Restrictions apply.

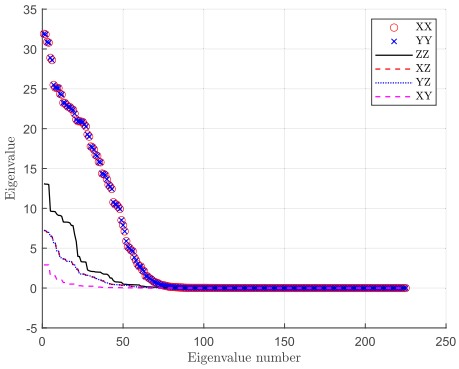

Fig. 9. Eigenvalues of the co-polarized and cross-polarized HMIMOS wireless channels for a single user lying in the NF regime ($z = 3\lambda$).

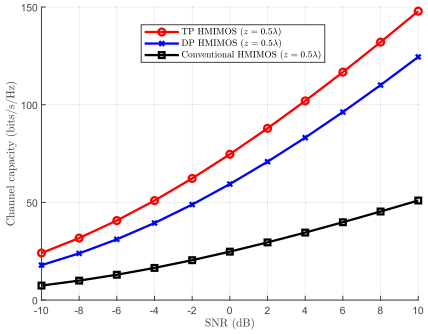

(a) Channel capacity v.s. SNR

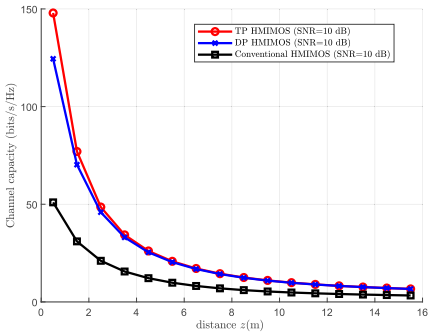

(b) Channel capacity v.s. distance z

Fig. 10. The channel capacity of a TP HMIMOS, DP HMIMOS, and conventional HMIMOS systems.

dominant than zth co-polarized channel since they have more number of high value eigenvalues. This is accounted for that zth polarized component decays with the distance, and it even goes to zero in the far-field.

The channel capacity comparison of TP HMIMOS, DP HMIMOS [52], and the conventional HMIMOS equipped with single polarized patch antennas is demonstrated in Fig. 10. The wavelength $\lambda = 1$ m, the transmitter and receiver are equipped with 36 and 9 patch antennas, respectively, and the spacing between patch antennas is 0.4λ. In Fig. 10 (a), the single user is located at the distances $z = 0.5\lambda$. It can be observed that the TP HMIMOS has the largest capacity, since the full polarization is exploited, and the capacity grows as SNR increases. However, as the distance z between the transmitter and receivers increases, the gap between TP HMIMOS and DP HMIMOS decreases, as shown in Fig. 10 (b) with SNR $= 10$ dB. This showcases that the zth polarization component decays fast with the distance. It is thus apparent

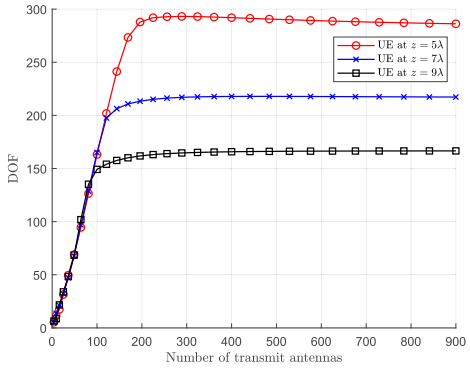

Fig. 11. DoF v.s. number of transmit antennas with the fixed surface at different users.

that the capacity of TP HMIMOS gradually coincides with the DP HMIMOS as the z distance increases.

B. Diversity Analysis in TP Systems

If the channel between N_s transmitter antennas and N_r receiver antennas is full-rank, the transmitted signal experiences $N_r N_s$ different paths, thus, the maximal diversity gain is $N_r N_s$ [53]. Considering that both spatial diversity and polarization diversity contribute to the systems diversity, TP systems can further improve the reliability of the communications. The diversity gain (DoF) is defined as [54]

$$\mathcal{D} = \left(\frac{\mathrm{tr}(\mathbf{R})}{|\mathbf{R}|_f} \right)^2, \tag{66}$$

where the transmit and receive correlation factors in $\mathbf{R}$ can be computed through (54).

The DoF of the generated channel with different number of transmit antennas is given in Fig. 11. The HMIMOS surface is $A_s = A_r = 100\lambda^2$ (square shape), and we consider three users located at $z = 5\lambda, 7\lambda$ and 9λ, respectively. It can be observed from the figure that the further users have a smaller DOF since the zth component decays fast with the distance. More importantly, the simulated curves all reach plateau, for example, the DoF of user at $z = 7\lambda$ ceases increasing when the number of transmit antennas exceeds 300, which reflects that increasing transmit antennas cannot improve the performance continuously. In other words, the DoF of the TP HMIMOS is performance limited.

The influence of HMIMOS shape on the DoF is given in Fig. 12. The HMIMOS surface is fixed as $A_s = A_r = 64\lambda^2$, and the user is located at $z = 5\lambda$. It can be observed from the figure that different shapes affects DoF. Specifically, the square shape has the largest DoF while the circle shape has a lower DoF. This is due to that the circle shape has a lower spacing between patch antennas and a higher correlation, thus generates a lower DoF than other shapes. This observation is similar to that in [40], which proposed that more antennas can be inserted inside a square than inside a circle without severely degrading diversity gain performance. In addition, the higher ratio between the long length and the short length has a lower DoF, e.g., the DoF of rectangle shape with $16\lambda \times 4\lambda$ is higher than $32\lambda \times 2\lambda$. This can be explained by that the number of

Authorized licensed use limited to: Zhejiang University. Downloaded on December 14,2023 at 13:10:36 UTC from IEEE Xplore. Restrictions apply.

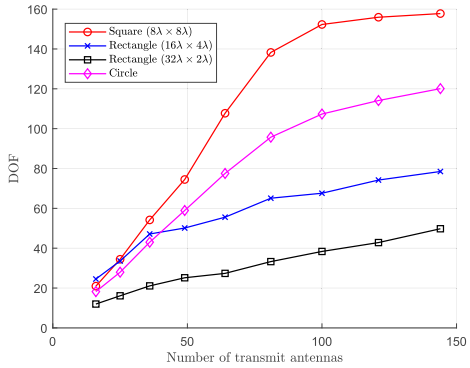

Fig. 12. DoF v.s. number of transmit antennas with the fixed surface for the user located at $z = 5\lambda$.

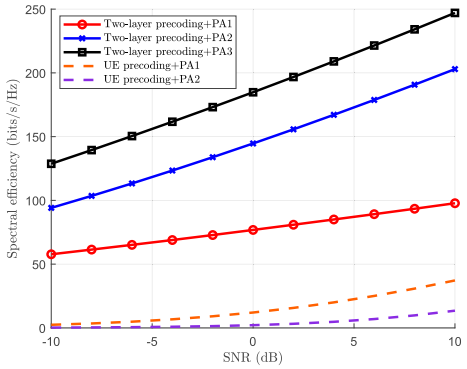

Fig. 13. Spectral efficiency of the two proposed precoding schemes with different PA schemes for $K = 3$ users.

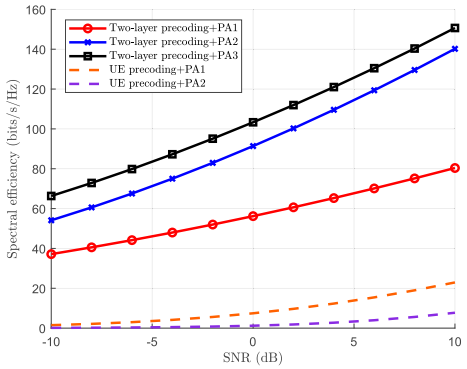

Fig. 14. Spectral efficiency of the two proposed precoding schemes with different PA schemes for $K = 6$ users.

vertical patch antennas is fixed, in which the shorter length produces higher spatial correlation, thus results in lower DoF.

C. Spectral Efficiency in TP System

Since the cross-polarization interference is eliminated through two-layer precoding schemes, the performance of systems is mainly affected by co-polarization components. The signal-to-interference-plus-noise ratio (SINR) for the kth patch antenna in ith ($i \in \{x, y, z\}$) polarization is

$$\mathrm{SINR}_{k,i} = \frac{Q_i G_{k,i} |\mathbf{H}^{\mathbf{F}}_{ii,k} \mathbf{p}_{i,k} x_{i,k}|^2}{Q_i |\mathbf{H}^{\mathbf{F}}_{ii,k} \sum_{k' \neq k}^{K} G_{k'} \mathbf{p}_{i,k'} x_{i,k'}|^2 + \sigma_w^2}, \quad (67)$$

where $\mathbf{H}^{\mathbf{F}}_{ii,k}$ is the channel matrix in the ith co-polarization for the kth patch antenna. Thus, the spectral efficiency of the ith co-polarization is

$$\mathcal{R}_{ii} = \log_2 |\mathbf{I} + \frac{Q_i \mathbf{G}_i \bar{\mathbf{\Lambda}}_i^2}{\sigma_w^2}| = \sum_{j=1}^{\mathrm{rank}(\bar{\mathbf{\Lambda}})} \log_2 |1 + \frac{Q_i G_{i,j} \bar{\lambda}_j^2}{\sigma_w^2}|, \quad (68)$$

where the matrix $\bar{\mathbf{\Lambda}}_i$ collects the singular values of the channel matrix for ith co-polarization, and $\mathbf{G}_i$ collects power for all users in the ith polarization.

The averaged spectral efficiency of different precoding schemes combining with different PA methods v.s. signal-to-noise ratio (SNR) for $K = 3$ users is shown in Fig. 13. The parameter setting $N_s = 225, \bar{N}_r = 36, \Delta_x^r = \Delta_x^s = 0.4\lambda$ and $K = 3$ users are located at $z = \lambda, 3\lambda$ and 5λ, respectively. It can be observed from Fig. 13 that the user-cluster-based method (denoted as UE precoding) is outperformed by the two-layer precoding scheme. This happens because only one third of the polarization diversity is utilized in the former method. In addition, the two-layer precoding scheme with the two-layer PA method shows the highest spectral efficiency while the polarization selection based PA method has the lowest spectral efficiency. This is due to that three polarized channels are fully exploited in the former case while only one polarized channel is employed in the latter case.

The averaged spectral efficiency of different precoding schemes combining with different PA methods v.s. SNR given $K = 6$ users is shown in Fig. 14. The parameter setting $N_s = 225, \bar{N}_r = 36, \Delta_x^r = \Delta_x^s = 0.4\lambda$ and 6 users are located at $z = \lambda, 2\lambda, 3\lambda, 4\lambda, 5\lambda$, and 6λ, respectively. Through the comparison between Fig. 13 and Fig. 14, the averaged spectral efficiency of both precoding schemes decreases as the user number grows. In addition, in the two-layer precoding scheme, the gap between PA2 and PA3 is smaller in $K = 6$ users than that in $K = 3$ users. This can be explained by that the channel singularity reduces when the number of users grows, thus the performance gap between PA2 and PA3 decreases.

VII. Conclusion

This paper presented a NF channel model for TP MU HMIMOS-based wireless communication systems, which was based on the dyadic Green's function. The proposed channel model was used to design a user-cluster-based precoding scheme and a two-layer precoding scheme for mitigating cross-polarization and inter-user interferences, which are indispensable components in polarized systems. The theoretical correlation analysis in the NF region demonstrates that the space and distance have opposite effects on correlation. Our simulation results showcased that the considered TP-based systems have higher channel capacity than both DP-based and conventional HMIMOS systems in the NF regime, however, this superiority gradually vanishes in the far-field regime as the zth polarized components disappear. In addition, it was shown that when increasing the number of transmit antennas, one gradually reaches the DoF limit, while the shape of the HMIMOS also has a big effect on the achievable DoF. Furthermore, since the proposed two-layer precoding scheme combined with two-layer PA fully exploits the three polarizations to handle the power imbalance, it was verified that it always yields the best spectral efficiency among the compared precoding schemes. In the future, we intend to study the polarization mismatch loss and the impact of imperfect channel knowledge

Authorized licensed use limited to: Zhejiang University. Downloaded on December 14,2023 at 13:10:36 UTC from IEEE Xplore. Restrictions apply.

on the proposed methods when considering realistic scenarios. We also plan to capitalize on the cavity-model theory for the considered channel modeling problem and analyze the envelope correlation coefficients.

ACKNOWLEDGMENT

Any opinions, findings, and conclusions or recommendations expressed in this material are those of the author(s) and do not reflect the views of the Ministry of Education, Singapore.

REFERENCES

[1] B. Ning, Z. Chen, W. Chen, Y. Du, and J. Fang, "Terahertz multi-user massive MIMO with intelligent reflecting surface: Beam training and hybrid beamforming," *IEEE Trans. Veh. Technol.*, vol. 70, no. 2, pp. 1376–1393, Feb. 2021.

[2] I. F. Akyildiz, C. Han, and S. Nie, "Combating the distance problem in the millimeter wave and terahertz frequency bands," *IEEE Commun. Mag.*, vol. 56, no. 6, pp. 102–108, Jun. 2018.

[3] N. Shlezinger, G. C. Alexandropoulos, M. F. Imani, Y. C. Eldar, and D. R. Smith, "Dynamic metasurface antennas for 6G extreme massive MIMO communications," *IEEE Wireless Commun.*, vol. 28, no. 2, pp. 106–113, Apr. 2021.

[4] D. Dardari and N. Decarli, "Holographic communication using intelligent surfaces," *IEEE Commun. Mag.*, vol. 59, no. 6, pp. 35–41, Jun. 2021.

[5] J. Xu, L. You, G. C. Alexandropoulos, X. Yi, W. Wang, and X. Gao, "Near-field wideband extremely large-scale MIMO transmission with holographic metasurface antennas," 2022, *arXiv:2205.02533*.

[6] L. You, J. Xu, G. C. Alexandropoulos, J. Wang, W. Wang, and X. Gao, "Energy efficiency maximization of massive MIMO communications with dynamic metasurface antennas," *IEEE Trans. Wireless Commun.*, vol. 22, no. 1, pp. 393–407, Jan. 2023.

[7] C. Huang et al., "Holographic MIMO surfaces for 6G wireless networks: Opportunities, challenges, and trends," *IEEE Wireless Commun.*, vol. 27, no. 5, pp. 118–125, Oct. 2020.

[8] Y. Yuan, Q. Gu, A. Wang, D. Wu, and Y. Li, "Recent progress in research and development of reconfigurable intelligent surface," *ZTE Commun.*, vol. 20, no. 1, pp. 3–13, 2022.

[9] T. L. Marzetta, "Spatially-stationary propagating random field model for massive MIMO small-scale fading," in *Proc. IEEE ISIT*, Jun. 2018, pp. 391–395.

[10] A. Pizzo, L. Sanguinetti, and T. L. Marzetta, "Spatial characterization of electromagnetic random channels," *IEEE Open J. Commun. Soc.*, vol. 3, pp. 847–866, 2022.

[11] C. Huang, A. Zappone, G. C. Alexandropoulos, M. Debbah, and C. Yuen, "Reconfigurable intelligent surfaces for energy efficiency in wireless communication," *IEEE Trans. Wireless Commun.*, vol. 18, no. 8, pp. 4157–4170, Aug. 2019.

[12] L. Wei, C. Huang, G. C. Alexandropoulos, C. Yuen, Z. Zhang, and M. Debbah, "Channel estimation for RIS-empowered multi-user MISO wireless communications," *IEEE Trans. Commun.*, vol. 69, no. 6, pp. 4144–4157, Jun. 2021.

[13] L. Wei et al., "Joint channel estimation and signal recovery for RIS-empowered multiuser communications," *IEEE Trans. Commun.*, vol. 70, no. 7, pp. 4640–4655, Jul. 2022.

[14] E. C. Strinati et al., "Reconfigurable, intelligent, and sustainable wireless environments for 6G smart connectivity," *IEEE Commun. Mag.*, vol. 59, no. 10, pp. 99–105, Oct. 2021.

[15] L. Wei et al., "Multi-user holographic MIMO surfaces: Channel modeling and spectral efficiency analysis," *IEEE J. Sel. Topics Signal Process.*, vol. 16, no. 5, pp. 1112–1124, Aug. 2022.

[16] R. J. Williams, E. de Carvalho, and T. L. Marzetta, "A communication model for large intelligent surfaces," in *Proc. IEEE ICC Workshops*, Jun. 2020, pp. 1–6.

[17] S. Basharat, S. Hassan, H. Pervaiz, A. Mahmood, Z. Ding, and M. Gidlund, "Reconfigurable intelligent surfaces: Potentials, applications, and challenges for 6G wireless networks," *IEEE Wireless Commun.*, vol. 28, no. 6, pp. 184–191, Dec. 2021.

[18] E. Björnson and L. Sanguinetti, "Rayleigh fading modeling and channel hardening for reconfigurable intelligent surfaces," *IEEE Wireless Commun. Lett.*, vol. 10, no. 4, pp. 830–834, Apr. 2021.

[19] G. C. Alexandropoulos, N. C. Sagias, and K. Berberidis, "On the multivariate Weibull fading model with arbitrary correlation matrix," *IEEE Antennas Wireless Propag. Lett.*, vol. 6, pp. 93–95, 2007.

[20] G. C. Alexandropoulos, P. T. Mathiopoulos, and N. C. Sagias, "Switch-and-examine diversity over arbitrarily correlated Nakagami-m fading channels," *IEEE Trans. Veh. Technol.*, vol. 59, no. 4, pp. 2080–2087, May 2010.

[21] G. C. Alexandropoulos and P. T. Mathiopoulos, "Performance evaluation of selection diversity receivers over arbitrarily correlated generalised Gamma fading channels," *IET Commun.*, vol. 4, no. 10, pp. 1253–1265, Jun. 2010.

[22] S. S. A. Yuan, Z. He, X. Chen, C. Huang, and W. E. I. Sha, "Electromagnetic effective degree of freedom of an MIMO system in free space," *IEEE Antennas Wireless Propag. Lett.*, vol. 21, no. 3, pp. 446–450, Mar. 2022.

[23] D. Dardari, "Communicating with large intelligent surfaces: Fundamental limits and models," *IEEE J. Sel. Areas Commun.*, vol. 38, no. 11, pp. 2526–2537, Nov. 2020.

[24] A. S. de Sena et al., "IRS-assisted massive MIMO-NOMA networks: Exploiting wave polarization," *IEEE Trans. Wireless Commun.*, vol. 20, no. 11, pp. 7166–7183, Nov. 2021.

[25] M. Coldrey, "Modeling and capacity of polarized MIMO channels," in *Proc. VTC Spring*, May 2008, pp. 440–444.

[26] X. Chen et al., "Design and implementation of MIMO transmission based on dual-polarized reconfigurable intelligent surface," *IEEE Wireless Commun. Lett.*, vol. 10, no. 10, pp. 2155–2159, Oct. 2021.

[27] Y. Han, X. Li, W. Tang, S. Jin, Q. Cheng, and T. J. Cui, "Dual-polarized RIS-assisted mobile communications," *IEEE Trans. Wireless Commun.*, vol. 21, no. 1, pp. 591–606, Jan. 2022.

[28] A. S. de Sena, P. H. J. Nardelli, D. B. D. Costa, U. S. Dias, P. Popovski, and C. B. Papadias, "Dual-polarized IRSs in uplink MIMO-NOMA networks: An interference mitigation approach," *IEEE Wireless Commun. Lett.*, vol. 10, no. 10, pp. 2284–2288, Oct. 2021.

[29] G. Zafari, M. Koca, and H. Sari, "Dual-polarized spatial modulation over correlated fading channels," *IEEE Trans. Commun.*, vol. 65, no. 3, pp. 1336–1352, Mar. 2017.

[30] S. Sugiura, Y. Kawai, T. Matsui, T. Lee, and H. Iizuka, "Joint beam and polarization forming of intelligent reflecting surfaces for wireless communications," *IEEE Trans. Veh. Technol.*, vol. 70, no. 2, pp. 1648–1657, Feb. 2021.

[31] S. Nie and I. F. Akyildiz, "Codebook design for dual-polarized ultra-massive MIMO communications at millimeter wave and terahertz bands," in *Proc. ICASSP*, Jun. 2021, pp. 8072–8076.

[32] Y. Xu, Z. Yang, C. Huang, C. Yuen, and G. Gui, "Resource allocation for two-tier RIS-assisted heterogeneous NOMA networks," *ZTE Commun.*, vol. 20, no. 1, pp. 36–47, 2022.

[33] T. Oh, Y.-G. Lim, C.-B. Chae, and Y. Lee, "Dual-polarization slot antenna with high cross-polarization discrimination for indoor small-cell MIMO systems," *IEEE Antennas Wireless Propag. Lett.*, vol. 14, pp. 374–377, 2015.

[34] M. Jian et al., "Reconfigurable intelligent surfaces for wireless communications: Overview of hardware designs, channel models, and estimation techniques," *Intell. Converged Netw.*, vol. 3, no. 1, pp. 1–32, Mar. 2022.

[35] E. Ibrahim, R. Nilsson, and J. Van De Beek, "Binary polarization shift keying with reconfigurable intelligent surfaces," *IEEE Wireless Commun. Lett.*, vol. 11, no. 5, pp. 908–912, May 2022.

[36] M. R. Alam, K. M. Muttaqi, and T. K. Saha, "Classification and localization of fault-initiated voltage sags using 3-D polarization ellipse parameters," *IEEE Trans. Power Del.*, vol. 35, no. 4, pp. 1812–1822, Aug. 2020.

[37] T. Carozzi, R. L. Karlsson, and J. Bergman, "Parameters characterizing electromagnetic wave polarization," *Phys. Rev. E, Stat. Phys. Plasmas Fluids Relat. Interdiscip. Top.*, vol. 61, pp. 2024–2028, Feb. 2000. [Online]. Available: https://link.aps.org/doi/10.1103/PhysRevE.61.2024

[38] S. M. Mikki and Y. M. M. Antar, "A theory of antenna electromagnetic near field—Part II," *IEEE Trans. Antennas Propag.*, vol. 59, no. 12, pp. 4706–4724, Dec. 2011.

[39] H. F. Arnoldus, "Representation of the near-field, middle-field, and far-field electromagnetic Green's functions in reciprocal space," *J. Opt. Soc. Amer. B, Opt. Phys.*, vol. 18, no. 4, pp. 547–555, 2001.

[40] S. M. Mikki, S. Clauzier, and Y. M. M. Antar, "Empirical geometrical bounds on MIMO antenna arrays for optimum diversity gain performance: An electromagnetic design approach," *IEEE Access*, vol. 6, pp. 39876–39894, 2018.

Authorized licensed use limited to: Zhejiang University. Downloaded on December 14,2023 at 13:10:36 UTC from IEEE Xplore. Restrictions apply.

[41] K. B. Ocheltree and L. A. Frizzel, "Sound field calculation for rectangular sources," *IEEE Trans. Ultrason., Ferroelectr., Freq. Control*, vol. 36, no. 2, pp. 242–248, Mar. 1989.
[42] R. C. Johnson, H. A. Ecker, and J. S. Hollis, "Determination of far-field antenna patterns from near-field measurements," *Proc. IEEE*, vol. 61, no. 12, pp. 1668–1694, Dec. 1973.
[43] M. Cui, Z. Wu, Y. Lu, X. Wei, and L. Dai, "Near-field communications for 6G: Fundamentals, challenges, potentials, and future directions," 2022, *arXiv:2203.16318*.
[44] M. Peng, X. Zhang, W. Wang, and H.-H. Chen, "Performance of dual-polarized MIMO for TD-HSPA evolution systems," *IEEE Syst. J.*, vol. 5, no. 3, pp. 406–416, Sep. 2011.
[45] B. Cao, A.-J. Liu, X.-P. Mao, and Q.-Y. Zhang, "An oblique projection polarization filter," in *Proc. 4th Int. Conf. Wireless Commun., Netw. Mobile Comput.*, Oct. 2008, pp. 1–4.
[46] G. C. Raleigh and J. M. Cioffi, "Spatio-temporal coding for wireless communication," *IEEE Trans. Commun.*, vol. 46, no. 3, pp. 357–366, Mar. 1998.
[47] J. Zhang, R. Chen, J. G. Andrews, A. Ghosh, and R. W. Heath Jr., "Networked MIMO with clustered linear precoding," *IEEE Trans. Wireless Commun.*, vol. 8, no. 4, pp. 1910–1921, Apr. 2009.
[48] Q. H. Spencer, A. L. Swindlehurst, and M. Haardt, "Zero-forcing methods for downlink spatial multiplexing in multiuser MIMO channels," *IEEE Trans. Signal Process.*, vol. 52, no. 2, pp. 461–471, Feb. 2004.
[49] C. Henkel, K. Joulain, R. Carminati, and J.-J. Greffet, "Spatial coherence of thermal near fields," *Opt. Commun.*, vol. 186, nos. 1–3, pp. 57–67, Dec. 2000. [Online]. Available: https://www.sciencedirect.com/science/article/pii/S0030401800010488
[50] W. C. Chew, W. E. I. Sha, and Q. I. Dai, "Green's dyadic, spectral function, local density of states, and fluctuation dissipation theorem," *Prog. Electromagn. Res.*, vol. 166, pp. 147–165, 2020.
[51] C. T. Tai and G. Eleftheriades, "Dyadic Green functions in electromagnetic theory," *IEEE Proc.*, vol. 83, no. 6, p. 998, Nov. 1995.
[52] A. Bhowal and S. Aissa, "Polarization-enabled MIMO bidirectional device-to-device communications via RIS," *IEEE Trans. Commun.*, vol. 71, no. 1, pp. 427–440, Jan. 2023.
[53] L. Zheng and D. N. C. Tse, "Diversity and multiplexing: A fundamental tradeoff in multiple-antenna channels," *IEEE Trans. Inf. Theory*, vol. 49, no. 5, pp. 1073–1096, May 2003.
[54] S. M. Mikki and Y. M. M. Antar, "On cross correlation in antenna arrays with applications to spatial diversity and MIMO systems," *IEEE Trans. Antennas Propag.*, vol. 63, no. 4, pp. 1798–1810, Apr. 2015.

Li Wei (Graduate Student Member, IEEE) received the B.S. degree in communication engineering from Southwest Jiaotong University, China, in 2015, and the M.S. degree in electronic and communication engineering from Xidian University, China, in 2019. She is currently pursuing the Ph.D. degree with the Engineering Product Development (EPD) Pillar, Singapore University of Technology and Design, Singapore. Her research interests include reconfigurable intelligent surfaces and signal processing for wireless communications.

Chongwen Huang (Member, IEEE) received the B.Sc. degree from Nankai University in 2010, the M.Sc. degree from the University of Electronic Science and Technology of China in 2013, and the Ph.D. degree from the Singapore University of Technology and Design (SUTD) in 2019. From October 2019 to September 2020, he was a Post-Doctoral Researcher with SUTD. Since September 2020, he has been with Zhejiang University, as a tenure-track young Professor. His main research interests include holographic MIMO surface/reconfigurable intelligent surface, B5G/6G wireless communication, mmWave/THz communications, and deep learning technologies for wireless communications. He was a recipient of the IEEE Marconi Prize Paper Award in wireless communications and the IEEE ComSoc Asia–Pacific Outstanding Young Researcher Award in 2021. He has been serving as an Editor for IEEE COMMUNICATIONS LETTER, *Signal Processing* (Elsevier), *EURASIP Journal on Wireless Communications and Networking*, and *Physical Communication*, since 2021.

George C. Alexandropoulos (Senior Member, IEEE) received the Diploma degree in computer engineering and informatics (integrated M.Sc.), the M.A.Sc. degree in signal and communications processing systems, and the Ph.D. degree in wireless communications from the School of Engineering, University of Patras, Greece, in 2003, 2005, and 2010, respectively. He has held a senior research positions at various Greek universities and research institutes. He was a Senior Research Engineer and a Principal Researcher with the Mathematical and Algorithmic Sciences Laboratory, Paris Research Center, Huawei Technologies France; and the Technology Innovation Institute, Abu Dhabi, United Arab Emirates, respectively. He is currently an Assistant Professor with the Department of Informatics and Telecommunications, School of Sciences, National and Kapodistrian University of Athens (NKUA), Greece. He is and has been involved in the organization of various special sessions and workshops at flagship IEEE conferences. He has participated and/or technically managed more than 15 European Union (EU), international, and Greek research, innovation, and development projects. He is currently a NKUA's Principal Investigator for the EU H2020 RISE-6G and the SNS JU TERRAMETA projects dealing with RIS-empowered smart wireless environments and THz RISs, respectively. For the former project, he also serves as the dissemination manager, whereas, for the latter, as the technical manager. His research interests span the general areas of algorithmic design and performance analysis for wireless networks, with an emphasis on multi-antenna transceiver hardware architectures, full duplex radios, active and passive reconfigurable intelligent surfaces (RISs), integrated communications and sensing, millimeter wave and THz communications, and distributed machine learning algorithms. He is a Senior Member of the IEEE Communications, Signal Processing, and Information Theory Societies, the Vice Chair of the EURASIP Technical Area Committee on Signal Processing for Communications and Networking, and a registered Professional Engineer of the Technical Chamber of Greece. He has received the Best Ph.D. Thesis Award in 2010, the IEEE Communications Society Best Young Professional in Industry Award in 2018, the EURASIP Best Paper Award of the *Journal on Wireless Communications and Networking* in 2021, the IEEE Marconi Prize Paper Award in Wireless Communications in 2021, and the Best Paper Award from the IEEE GLOBECOM 2021. He currently serves as an Editor for IEEE TRANSACTIONS ON COMMUNICATIONS, IEEE WIRELESS COMMUNICATIONS LETTERS, *Frontiers in Communications and Networks*, and the *ITU Journal on Future and Evolving Technologies*. In the past, he has held various fixed-term and a guest editorial positions of IEEE TRANSACTIONS ON WIRELESS COMMUNICATIONS, IEEE COMMUNICATIONS LETTERS, and *Computer Networks* (Elsevier), and for various special issues at IEEE journals. He is also a Distinguished Lecturer of the IEEE Communications Society. For more information visit the link (www.alexandropoulos.info).

Zhaohui Yang (Member, IEEE) received the Ph.D. degree from Southeast University, Nanjing, China, in 2018. From 2018 to 2020, he was a Post-Doctoral Research Associate with the Department of Informatics, Center for Telecommunications Research, King's College London, U.K. From 2020 to 2022, he was a Research Fellow with the Department of Electronic and Electrical Engineering, University College London, U.K. He is currently a ZJU Young Professor with the Zhejiang Key Laboratory of Information Processing Communication and Networking, College of Information Science and Electronic Engineering, Zhejiang University; and a Research Scientist with the Zhejiang Laboratory. His research interests include joint communication, sensing, and computation, federated learning, and semantic communication. He was the Co-Chair of international workshops with more than 10 times, including IEEE ICC, IEEE GLOBECOM, IEEE WCNC, IEEE PIMRC, and IEEE INFOCOM. He is an Associate Editor of the IEEE COMMUNICATIONS LETTERS, *IET Communications*, and *EURASIP Journal on Wireless Communications and Networking*. He has served as a Guest Editor for several journals, including IEEE JOURNAL ON SELECTED AREAS IN COMMUNICATIONS.

Authorized licensed use limited to: Zhejiang University. Downloaded on December 14,2023 at 13:10:36 UTC from IEEE Xplore. Restrictions apply.

Jun Yang received the B.S. degree in geophysics from the China University of Geosciences, Wuhan, in 2011, and the Joint-Training Ph.D. degree in geophysics from the University of Science and Technology of China and the University of North Carolina at Charlotte, in 2016. He is currently an Algorithm Engineer with ZTE Corporation. His research interests include reconfigurable intelligent surface, MIMO channel modeling, and computational electromagnetics.

Wei E. I. Sha (Senior Member, IEEE) received the B.S. and Ph.D. degrees in electronic engineering from Anhui University, Hefei, China, in 2003 and 2008, respectively. From July 2008 to July 2017, he was a Post-Doctoral Research Fellow and then a Research Assistant Professor with the Department of Electrical and Electronic Engineering, The University of Hong Kong, Hong Kong. From March 2018 to March 2019, he was with University College London, London, U.K., as a Marie-Curie Individual Fellow. In October 2017, he joined the College of Information Science and Electronic Engineering, Zhejiang University, Hangzhou, China, where he is currently a tenure-tracked Assistant Professor. He has authored or coauthored 190 refereed journal articles, 150 conference publications, nine book chapters, and two books. His Google Scholar citation is 8578 with an H-index of 46. His research interests include theoretical and computational research in electromagnetics, focusing on the multiphysics and interdisciplinary research. He served as a reviewer for 60 technical journals and a technical program committee member of ten IEEE conferences. He was awarded the Second Prize of Science and Technology from Anhui Province Government, China, in 2015; and the Technical Achievement Award of Applied Computational Electromagnetics Society (ACES) in 2022. He also received seven best student paper prizes with his students. He also served as an Associate Editor for IEEE JOURNAL ON MULTISCALE AND MULTI PHYSICS COMPUTATIONAL TECHNIQUES, IEEE OPEN JOURNAL OF ANTENNAS AND PROPAGATION, and IEEE ACCESS.

Zhaoyang Zhang (Senior Member, IEEE) received the Ph.D. degree from Zhejiang University, Hangzhou, China, in 1998. He is currently a Qiushi Distinguished Professor with Zhejiang University. He has coauthored more than 400 peer-reviewed international journal and conference papers, including eight conference best papers awarded by IEEE ICC 2019 and IEEE Globecom 2020. His research interests include the fundamental aspects of wireless communications and networking, such as information theory and coding theory, network signal processing and distributed learning, AI-empowered communications and networking, synergetic sensing, and computing and communication.

He was awarded the National Natural Science Fund for Distinguished Young Scholar by NSFC in 2017. He was the General Chair and the TPC Co-Chair or the Symposium Co-Chair of PIMRC 2021 Workshop on Native AI Empowered Wireless Networks, VTC-Spring 2017 Workshop on HMWC, WCSP 2013/2018, and Globecom 2014 Wireless Communications Symposium. He was also a Keynote Speaker of IEEE Globecom 2021 Workshop on Native-AI Wireless, APCC 2018, and VTC-Fall 2017 Workshop on NOMA. He is serving or has served as an Editor for IEEE TRANSACTIONS ON WIRELESS COMMUNICATIONS, IEEE TRANSACTIONS ON COMMUNICATIONS, and *IET Communications*.

Mérouane Debbah (Fellow, IEEE) received the M.Sc. and Ph.D. degrees from the Ecole Normale Supérieure Paris-Saclay, France. He was with Motorola Labs, Saclay, France, from 1999 to 2002; and the Vienna Research Center for Telecommunications, Vienna, Austria, until 2003. From 2003 to 2007, he was an Assistant Professor with the Mobile Communications Department, Institut Eurecom, Sophia Antipolis, France. In 2007, he was appointed as a Full Professor with Centrale Supélec, Gif-sur-Yvette, France. From 2007 to 2014, he was the Director of the Alcatel-Lucent Chair on Flexible Radio. From 2014 to 2021, he was the Vice-President of the Huawei France Research Center. He was jointly the Director of the Mathematical and Algorithmic Sciences Laboratory and the Lagrange Mathematical and Computing Research Center. Since 2021, he has been leading the AI and Digital Science Research Center, Technology Innovation Institute. He is a Chief Researcher with the Technology Innovation Institute, Abu Dhabi. He is also an Adjunct Professor with the Department of Machine Learning, Mohamed Bin Zayed University of Artificial Intelligence. He has managed eight EU projects and more than 24 national and international projects. His research interests lie in fundamental mathematics, algorithms, statistics, information, and communication sciences research. He is a WWRF Fellow, a Eurasip Fellow, an AAIA Fellow, an Institut Louis Bachelier Fellow, and a Membreé mérite SEE. He was a recipient of the ERC Grant MORE (Advanced Mathematical Tools for Complex Network Engineering) from 2012 to 2017. He was also a recipient of the Mario Boella Award in 2005, the IEEE Glavieux Prize Award in 2011, the Qualcomm Innovation Prize Award in 2012, the 2019 IEEE Radio Communications Committee Technical Recognition Award, and the 2020 SEE Blondel Medal. He received more than 20 best paper awards, including the 2007 IEEE GLOBECOM Best Paper Award, the Wi-Opt 2009 Best Paper Award, the 2010 Newcom++ Best Paper Award, the WUN CogCom Best Paper 2012 and 2013 Award, the 2014 WCNC Best Paper Award, the 2015 ICC Best Paper Award, the 2015 IEEE Communications Society Leonard G. Abraham Prize, the 2015 IEEE Communications Society Fred W. Ellersick Prize, the 2016 IEEE Communications Society Best Tutorial Paper Award, the 2016 European Wireless Best Paper Award, the 2017 Eurasip Best Paper Award, the 2018 IEEE Marconi Prize Paper Award, the 2019 IEEE Communications Society Young Author Best Paper Award, the 2021 Eurasip Best Paper Award, the 2021 IEEE Marconi Prize Paper Award, the 2022 IEEE Communications Society Outstanding Paper Award, the 2022 ICC Best paper Award, the Valuetools 2007, Valuetools 2008, CrownCom 2009, Valuetools 2012, SAM 2014, and the 2017 IEEE Sweden VT-COM-IT Joint Chapter Best Student Paper Awards. He is the Associate Editor-in-Chief of the *Random Matrix: Theory and Applications* journal. He was an Associate Area Editor and a Senior Area Editor of the IEEE TRANSACTIONS ON SIGNAL PROCESSING, from 2011 to 2013 and from 2013 to 2014, respectively. From 2021 to 2022, he serves as an IEEE Signal Processing Society Distinguished Industry Speaker.

Chau Yuen (Fellow, IEEE) received the B.Eng. and Ph.D. degrees from Nanyang Technological University, Singapore, in 2000 and 2004, respectively.

He was a Post-Doctoral Fellow with Lucent Technologies Bell Labs, Murray Hill, in 2005, and a Visiting Assistant Professor with The Hong Kong Polytechnic University in 2008. From 2006 to 2010, he was with the Institute for Infocomm Research, Singapore. From 2010 to 2023, he was with the Engineering Product Development Pillar, Singapore University of Technology and Design. Since 2023, he has been with the School of Electrical and Electronic Engineering, Nanyang Technological University. He has three U.S. patents and published over 500 research papers at international journals or conferences.

Dr. Yuen was a recipient of the Lee Kuan Yew Gold Medal, the Institution of Electrical Engineers Book Prize, the Institute of Engineering of Singapore Gold Medal, the Merck Sharp and Dohme Gold Medal, and the Hewlett Packard Prize (twice). He received the IEEE Asia–Pacific Outstanding Young Researcher Award in 2012 and IEEE VTS Singapore Chapter Outstanding Service Award on 2019. He was awarded as the IEEE TRANSACTIONS ON NETWORK SCIENCE AND ENGINEERING Excellent Editor Award and the Top Associate Editor for IEEE TRANSACTIONS ON VEHICULAR TECHNOLOGY from 2009 to 2015. He currently serves as the Editor-in-Chief for *Nature Computer Science* (Springer); and an editor for IEEE TRANSACTIONS ON VEHICULAR TECHNOLOGY, IEEE SYSTEMS JOURNAL, and IEEE TRANSACTIONS ON NETWORK SCIENCE AND ENGINEERING. He also served as the Guest Editor for several special issues, including IEEE JOURNAL ON SELECTED AREAS IN COMMUNICATIONS, *IEEE Wireless Communications Magazine*, *IEEE Communications Magazine*, *IEEE Vehicular Technology Magazine*, IEEE TRANSACTIONS ON COGNITIVE COMMUNICATIONS AND NETWORKING, and *Applied Energy* (Elsevier). He is a Distinguished Lecturer of IEEE Vehicular Technology Society and also a Highly Cited Researcher by Clarivate Web of Science.

Authorized licensed use limited to: Zhejiang University. Downloaded on December 14,2023 at 13:10:36 UTC from IEEE Xplore. Restrictions apply.